JGR Solid Earth

RESEARCH ARTICLE
10.1029/2021JB023160

Constraints on Crustal Structure in the Vicinity of the Adriatic Indenter (European Alps) From *Vp* and *Vp/Vs* Local Earthquake Tomography

Azam Jozi Najafabadi[1,2], Christian Haberland[1], Eline Le Breton[3], Mark R. Handy[3], Vincent F. Verwater[3,4], Benjamin Heit[1], Michael Weber[1], and the AlpArray and AlpArray SWATH-D Working Groups[5]

[1]GFZ German Research Centre for Geosciences, Potsdam, Germany, [2]Institute of Geosciences, Potsdam University, Potsdam, Germany, [3]Institute of Geological Sciences, Freie Universität Berlin, Berlin, Germany, [4]Now at Division of Transport & Mobility, Department of Geotechnical, Sweco Nederland B.V., De Bilt, The Netherlands, [5]See Appendix B

Key Points:

- *Vp* and *Vp/Vs* models of the crust and upper mantle were calculated in the Eastern and eastern Southern Alps using a high-quality data set
- The simultaneous inversion of 3-D velocity models and earthquake parameters were performed using the well-established SIMUL2000 algorithm
- The structure of Alpine orogenic crust including the tip of the Adriatic Indenter is revealed with the *Vp* model

Correspondence to:
A. Jozi Najafabadi,
azam@gfz-potsdam.de

Citation:
Jozi Najafabadi, A., Haberland, C., Le Breton, E., Handy, M. R., Verwater, V. F., Heit, B., et al. (2022). Constraints on crustal structure in the vicinity of the Adriatic Indenter (European Alps) from *Vp* and *Vp/Vs* local earthquake tomography. *Journal of Geophysical Research: Solid Earth*, *127*, e2021JB023160. https://doi.org/10.1029/2021JB023160

Received 2 SEP 2021
Accepted 3 FEB 2022

Abstract In this study, 3-D models of P-wave velocity (*Vp*) and P-wave and S-wave ratio (*Vp/Vs*) of the crust and upper mantle in the Eastern and eastern Southern Alps (northern Italy and southern Austria) were calculated using local earthquake tomography (LET). The data set includes high-quality arrival times from well-constrained hypocenters observed by the dense, temporary seismic networks of the AlpArray AASN and SWATH-D. The resolution of the LET was checked by synthetic tests and analysis of the model resolution matrix. The small inter-station spacing (average of ∼15 km within the SWATH-D network) allowed us to image crustal structure at unprecedented resolution across a key part of the Alps. The derived P velocity model revealed a highly heterogeneous crustal structure in the target area. One of the main findings is that the lower crust is thickened, forming a bulge at 30–50 km depth just south of and beneath the Periadriatic Fault and the Tauern Window. This indicates that the lower crust decoupled both from its mantle substratum as well as from its upper crust. The Moho, taken to be the iso-velocity contour of $Vp = 7.25$ km/s, agrees with the Moho depth from previous studies in the European and Adriatic forelands. It is shallower on the Adriatic side than on the European side. This is interpreted to indicate that the European Plate is subducted beneath the Adriatic Plate in the Eastern and eastern Southern Alps.

Plain Language Summary Energy released by earthquakes is converted to seismic waves that radiate through the Earth. Here, we study two types of waves (P and S) in the Eastern and eastern Southern Alps (northern Italy and southern Austria). The aim is to investigate the subsurface structure beneath the mountains. The P-wave and S-wave propagate at different velocities between the earthquakes and seismometers. Given the origin time and locations of earthquakes, seismometer coordinates, and wave arrival times, we can calculate the P-wave velocity (*Vp*) and the P-wave and S-wave velocity ratio (*Vp/Vs*) of the subsurface volume. Therefore, our velocity model allows for imaging the crust at unprecedented resolution. Moreover, an important structure within the Earth, the boundary between the crust and mantle or the so-called Moho, can be inferred by the study of the waves. Our results show that during collision and formation of the Eastern and eastern Southern Alps, the lower crust of the Adriatic Plate thickened due to decoupling from both the mantle and upper crust within the orogen. The Moho is shallower on the Adriatic side than on the European side. A possible interpretation is that the European Plate subducted under the Adriatic Plate in the Eastern and eastern Southern Alps.

1. Introduction

The Alpine chain was formed after the closure of Alpine Tethys and the collision of the continental parts of the Eurasian and African/Adriatic Plates (e.g., Handy et al., 2010; Le Breton et al., 2021; Schmid et al., 2004). The Alpine orogenic belt was modified when the northern edge of the Adriatic Plate indented the European Plate in Oligo-Miocene time (e.g., Ratschbacher et al., 1991; Scharf et al., 2013; Schmid et al., 1989; Schmid & Kissling, 2000). We define the part of the Adriatic Plate that has modified the Alpine orogenic edifice as "Adriatic Indenter." This indentation introduced heterogeneities into the structure of the crust and upper mantle under the Alps.

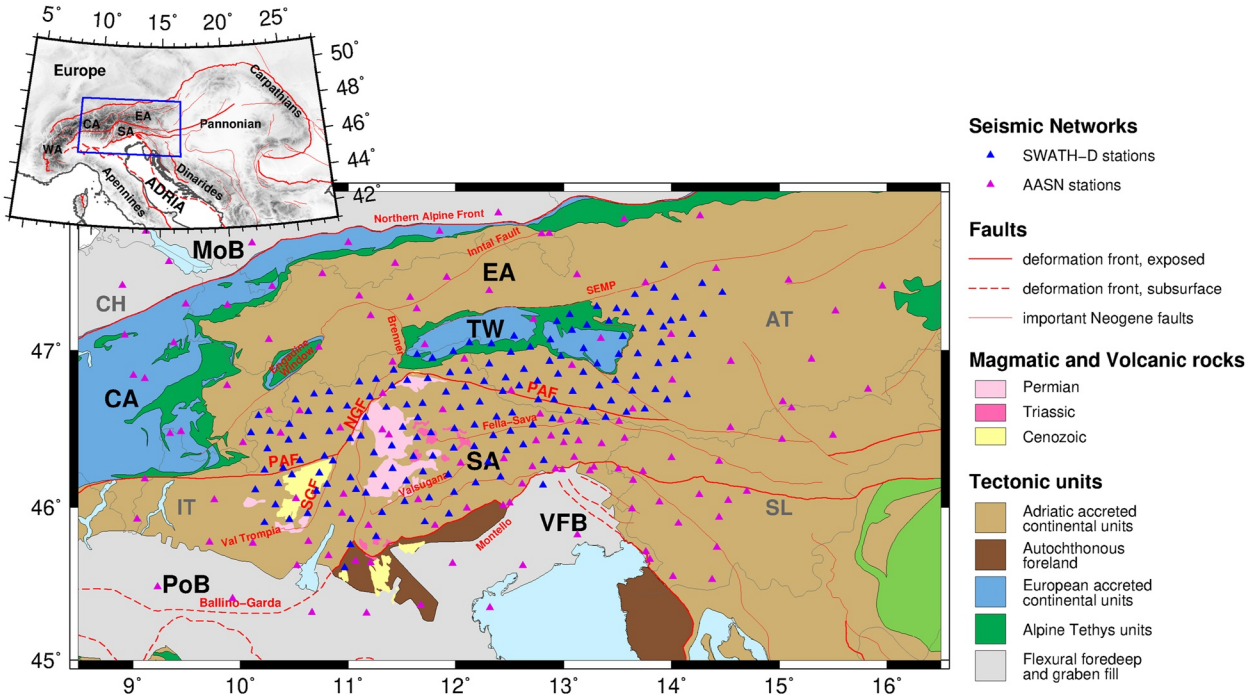

Figure 1. Tectonic map of the region showing major deformation fronts, faults, geographical subdivisions, and tectonic units modified after Schmid et al. (2004, 2008), Handy et al. (2010). Abbreviations: CA–Central Alps, EA–Eastern Alps, MoB–Molasse Basin, NGF–Northern Giudicarie Fault, PAF–Periadriatic Fault, PoB–Po Basin, SA–Southern Alps, SEMP–Salzach-Ennstal-Mariazell-Puchberg, SGF–Southern Giudicarie Fault, TW–Tauern Window, VFB–Venetian-Friuli Basin, WA–Western Alps, IT–Italy, SL–Slovenia, AT–Austria, CH–Switzerland.

The Eastern Alps comprise the Austroalpine nappes with Adriatic-derived crystalline basement rocks and sediments overlying accreted units, the so-called Penninic units, derived from Europe. The Periadriatic Fault (PAF; Figure 1) is a major dextral strike-slip fault delimiting the Eastern from the Southern Alps (Handy et al., 2006; Schmid et al., 1989). To the south of the PAF, the eastern Southern Alps are a S-directed fold-and-thrust belt affecting Mesozoic sedimentary cover and Permian magmatic rocks (Figure 1; Schuster & Stüwe, 2008; Tadiello & Braitenberg, 2021). The indentation of the Adriatic Plate resulted in orogen-parallel eastward lateral extrusion of the Eastern Alps toward the Pannonian Basin (e.g., Favaro et al., 2017; Horvath et al., 2006; Ratschbacher et al., 1991; Scharf et al., 2013). This was accommodated by dextral strike-slip along the PAF and also by N-S shortening in the Tauern Window (TW), which resulted in the exhumation of the highly metamorphic nappes of the European lower plate (e.g., Scharf et al., 2013). The PAF is offset sinistrally by the transverse Giudicarie Fault (Figure 1). The Northern Giudicarie Fault (NGF) is a Miocene sinistral strike-slip fault that forms an important boundary between distinctive orogenic styles in the west and east (e.g., Castellarin et al., 2006; Pomella et al., 2012, 2011; Verwater et al., 2021). To the east of the NGF (in the eastern Southern Alps), the Adriatic Plate still rotates counterclockwise with respect to the European Plate (e.g., Le Breton et al., 2017; Nocquet & Calis, 2004; Vrabec & Fodor, 2006; and refs therein).

In the Central Alps, the lower crust and upper mantle of the European Plate were subducted southward beneath the Adriatic Plate (e.g., Pfiffner et al., 1997; Schmid et al., 1996). It has been proposed that the lower crust of the Adriatic Plate is detached from its upper crust and mantle and forms a narrow wedge within the Central Alpine orogenic crust, which overlies the European lower crust (Diehl et al., 2009; Kissling et al., 2006; Rosenberg & Kissling, 2013; Schmid et al., 1996). To the east of the Giudicarie Fault (GF), along the N-S oriented TRANSALP geophysical transect of the Eastern Alps at about 12° longitude, most studies indicate a south-dipping European Moho dipping beneath the shallower Adriatic Moho (Castellarin et al., 2006; Gebrande et al., 2006; Kummerow et al., 2004; Lüschen et al., 2006). Gebrande et al. (2006) suggested an Adriatic lower crustal wedge indenting the European orogenic crust, similar to what had been established for the Central Alps (see Castellarin et al., 2006 for an overview). Questions remain on the exact extent of this potential Adriatic lower crustal wedge beneath the Eastern Alps and how it relates to the one proposed in the Central Alps.

East of the GF, teleseismic tomography of Lippitsch et al. (2003) indicated a positive *Vp* anomaly dipping NNE-ward to a depth varying from 150 km beneath the TW to 240 km further to the northeast at around 48°N/16°E. Together with the then-available models of Moho geometry (Waldhauser et al., 2002), this was interpreted as evidence for subduction of the Adriatic Plate beneath the European Plate. A first-order change in the subduction polarity somewhere beneath the transition from the Central to the Eastern Alps was thus proposed, which was initially supported by other seismological (Karousová et al., 2013; Kissling et al., 2006; Zhao et al., 2016) and geological studies (Handy et al., 2015; Kissling et al., 2006; Schmid et al., 2004). However, other studies, both before and since, do not favor a change in subduction polarity and postulate a single European slab beneath the Alps extending from west to east (Dando et al., 2011; Handy et al., 2021; Koulakov et al., 2009; Mitterbauer et al., 2011; Paffrath et al., 2021; Piromallo & Morelli, 2003). In recent interpretations, the part of the European slab beneath the Eastern Alps is largely detached from its orogenic lithosphere and dips southward in the Western Alps (~9°E) and sub-vertically to steeply northward in the Eastern Alps (~15°E; Handy et al., 2021; Paffrath et al., 2021).

Knowledge of the seismic velocity structure of the crust and upper mantle can improve tectonic models of the target area and provide information about the extent of the Adriatic lower crust and subduction polarity beneath the Central and Eastern Alps. The available seismic velocity models in the Alps are up to now either based on teleseismic tomography (e.g., Lippitsch et al., 2003; Mitterbauer et al., 2011; Paffrath et al., 2021) and thus cannot resolve the crustal structure or on the orogenic scale. Other models with local earthquakes as sources used less-dense seismic networks (e.g., Diehl et al., 2009; Solarino et al., 1997; Viganò et al., 2013) and thus have low resolution, hampering the detection of key crustal structures.

In this study, we present consistent 3-D Vp and Vp/Vs models of the Eastern and eastern Southern Alps derived from the inversion of a high-quality P and S travel-time data set based on Jozi Najafabadi et al. (2021). The high station density of the SWATH-D network (ca. 15 km spacing; Heit et al., 2017, 2021) allows for high-resolution images of the crustal structure in this part of the European Alps, even in a region of only moderate seismic activity. The seismic velocities (*Vp* and *Vs*) are influenced by the physical properties (e.g., density, porosity, fluid content, etc.) of the rocks. The *Vp* correlates positively with the density of the rock. Moreover, *Vp* and *Vs* are sensitive to the presence or absence of fluids, so that both *Vp* and *Vp*/*Vs* models provide information on the composition of the crust and mantle including possible partial melt.

The focus of our study is on the first-order features in the crust, especially on the extent of the lower crust beneath the Eastern Alps. Moreover, the crust-mantle discontinuity (Moho) in the target area is investigated in order to shed light on the subduction polarity beneath the Eastern Alps.

2. Local Earthquake Data

The waveform data used for this study was recorded by 161 stations of the temporary local SWATH-D network (Heit et al., 2017, 2021) and 112 selected stations of the larger scale AlpArray Seismic Network (AASN; Hetényi, Molinari, et al., 2018; Figure 1) from September 2017 to November 2019.

Jozi Najafabadi et al. (2021) analyzed a subset of this data (between September 2017 and the end of 2018) and generated a catalog of local earthquakes using the Markov chain Monte Carlo (McMC) approach, which uses a simultaneous inversion for hypocenters, station corrections, and the 1-D velocity structure (Ryberg & Haberland, 2019; see also; Kissling, 1988). In the current study, we complemented the catalog of Jozi Najafabadi et al. (2021) by collecting more network data (from January to November 2019) and analyzing them using the same procedure. The final catalog consists of 499 local earthquakes which closely resembles the seismicity shown in Jozi Najafabadi et al. (2021; their Figure 11).

The corresponding high-quality arrival-time data set was then utilized to perform the LET. The considered earthquakes have an azimuthal gap of less than 180° and at least 10 P and 5 S observations with a total of 16,484 P and 9,554 S picks (quality classes of 0–3; see Jozi Najafabadi et al., 2021 for more information). The average number of picks per event is 33 and 19 with average picking errors of 0.12 and 0.21 s for P and S observations, respectively (Table 1). More information on the number of P and S picks in each epicentral distance can be found in Figure A1.

Table 1
High-Quality P-Phase Data Set of 499 Local Earthquakes for LET and the Associated Picking Errors

Quality class	P picking uncertainty (s)	Number of P picks	S picking uncertainty (s)	Number of S picks
0	±0.05	6,510	±0.1	3,992
1	±0.1	5,020	±0.2	1,827
2	±0.2	3,414	±0.3	2,358
3	±0.3	1,540	±0.4	1,377
Sum (#)		16,484		9,554
Average picking error (s)		0.12		0.21

3. Tomographic Inversion

We utilized the well-established SIMUL2000 algorithm (Eberhart-Phillips & Michael, 1993; Evans et al., 1994; Thurber, 1983), one of the most widely used approaches for LET. SIMUL2000 inverts the travel-time residuals simultaneously for 3-D velocity structure (*Vp* and *Vp*/*Vs* models) and earthquake parameters. The inversion is performed using an iterative damped least-squares technique to solve the linearized, coupled hypocenter-velocity problem. The tomography solutions strongly depend on the choice of initial parameters (i.e., velocities and hypocenters), model parametrization, and regularization (i.e., damping values).

The model is formed by nodes on a regular grid. The SIMUL2000 code requires a 3-D seismic grid with initial *Vp* and *Vp*/*Vs* values associated with the nodes. The velocity between grid nodes is linearly interpolated (Thurber, 1983). The code comprises the solution of the forward problem (for the travel-times) as well, which is accomplished using a combination of approximate ray tracing (Thurber, 1983) and a pseudo-bending scheme (Um & Thurber, 1987).

3.1. Initial 1-D *Vp* and *Vp*/*Vs* Models

For the initial *Vp* values at seismic grid nodes, we adopted the 1-D model by Jozi Najafabadi et al. (2021) for the crust which was calculated using the McMC approach for a subset of the data used here. Since our data set was retrieved from a set of local earthquakes predominantly located in the upper crust (depth <20 km) and the number of large epicentral distances is limited (due to the relatively short network time frame of 2 years), the deeper levels (particularly the upper mantle) are less well-resolved. Accordingly, we decided to use the 1-D velocity model of Diehl et al. (2009) for greater depth (i.e., depths below 45 km) which shows higher velocities, representative for the upper mantle. For the initial *Vp*/*Vs* model, constant homogeneous values of 1.72 for the crust and 1.76 for the upper mantle (retrieved from the Wadati diagram) were used as an initial estimate. The initial *Vp* and *Vp*/*Vs* models at depth layers of our selected grid are given in Table 2 and Figure 2.

3.2. Model Parametrization and Inversion Scheme

Model resolution can be strongly affected by the model parametrization which should thus be carefully selected. A coarse parameterization yields highly resolved model nodes due to a large number of rays passing through a block of the grid. However, it can potentially overlook small features (smaller than the grid node spacing) in the subsurface, whereas a too fine parameterization yields less well resolved nodes and gives sparse images of subsurface structures.

Table 2
Initial 1-D P-Wave Velocities at Depth Layers of the Grid Used for LET

Depth (km)	*Vp* (km/s)	*Vp*/*Vs*
0	5.94	1.72
5	6.06	1.72
10	6.18	1.72
20	6.42	1.72
30	6.66	1.72
45	7.70	1.76
60	8.00	1.76
90	8.10	1.76

In the regions with variable ray sampling due to non-uniform earthquake and station distribution, some studies (Abers & Roecker, 1991; Bijwaard et al., 1998; Kissling, 1988; Thurber & Eberhart-Phillips, 1999) use uneven node spacing for enhancing ray sampling. These techniques give the possibility of using finer-scale parameterization where the data allows and improving the absolute model resolution by using a coarser grid where the ray coverage is sparser. However, the non-uniformity of the resolution within a given region could cause ambiguities in the interpretation of the velocity model, and velocity smearing between grid nodes might be interpreted as features.

Another strategy often used in regions with heterogeneous ray sampling is the graded inversion approach (Evans et al., 1994; Husen et al., 2000, 2003). In this approach, the inversion is first performed with a coarse parameterization and the obtained 3-D velocity model is then used as the initial model for another inversion with finer parameterization. This approach guarantees a smooth high-resolution velocity model throughout the volume

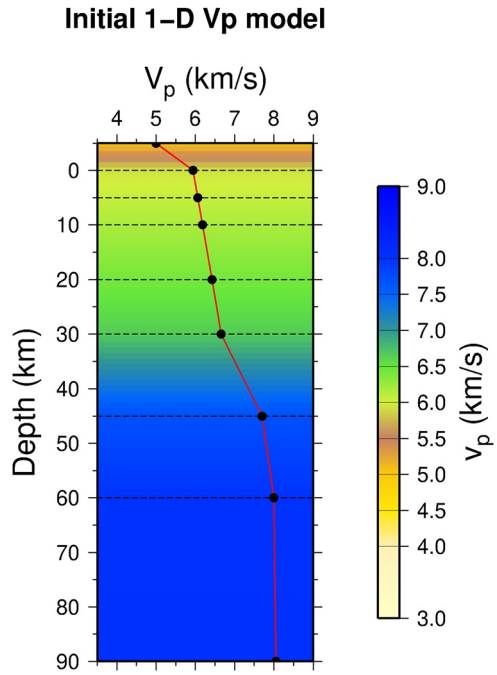

Figure 2. Initial 1-D P-wave velocities at depth layers of the grid used for LET.

with dense earthquake and station distribution without introducing artifacts (Eberhart-Phillips, 1990; Haberland et al., 2009; Husen et al., 2003).

After several tests with various approaches and parameterizations, we found the most appropriate model (also based on synthetic tests) using a graded scheme. The inversion with a coarse grid of 30 × 30 km^2 (horizontally) was initialized using the 1-D *Vp* model as described above (Section 3.1 and Table 2). Subsequently, the output 3-D velocity model was linearly interpolated (Thurber, 1983) into a finer grid of 15 × 15 km^2 (horizontally) and used as input for the next finer grid inversion. To adapt the retrieved anomalies after the inversion of the coarse grid, we shifted the nodes of the fine grid 7.5 km toward east and north, so that the nodes of the coarse grid are located between the nodes of the fine grid (see Figure 3). However, taking into account the very dense ray coverage only in the central part of the region (Figure 3), the grid cells in the periphery of the network were kept the same as the coarse parameterization. In both coarse and fine grid inversions, the vertical layer spacing is 5 km in the upper crust, 10 km in the lower crust, and 15 km in the upper mantle (Table 2 and Figure 2).

As for example, pointed out by Diehl (2008), due to the trade-off between model parametrization, minimum resolvable velocity perturbation, and average data error, parametrization plays an important role in resolution. A velocity perturbation with amplitude ΔV (%) within the volume of a grid block with a background velocity of $V0$ can be resolved only if the average picking error is less than the travel-time residual between the background model and the perturbed model. Given the data error of 0.12 s and a volume with Vp = 6 km/s, a 5% velocity perturbation (a rough estimation of what is expected in the upper crust of our study region) needs a ray length of at least ~15 km passing through the volume to be resolved (the reader is referred to the aforementioned publication for the mathematical formula). By assuming the ray length being almost equal to the volume dimension, our chosen parameterization of 15 × 15 × 10 km^3 can reliably resolve expected crustal structures with at least 5% velocity perturbations.

3.3. Regularization

The appropriate damping values of the inversions for *Vp* and *Vp*/*Vs* were determined by analyzing a series of single-iteration inversions and using a wide range of values. After inspection of the so-called trade-off curve (Eberhart-Phillips, 1986), the best compromise between data variance and model variance for *Vp* was obtained

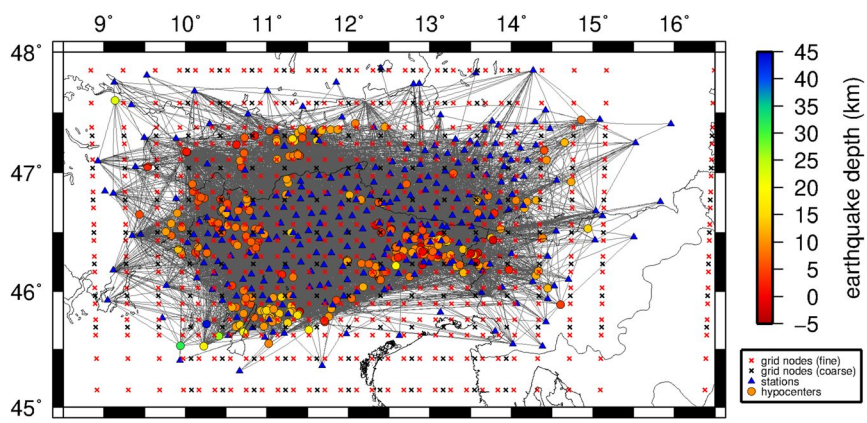

Figure 3. P-wave ray coverage of 499 local earthquakes and 273 stations. The black crosses show the grid nodes of the coarse parameterization (30-km horizontal spacing), and the red crosses illustrate the nodes of the fine grid (15-km horizontal spacing in the middle volume of the region). Note that at the periphery of the network the fine and coarse grids have the same node spacing and the red crosses are located on top of the black ones.

with damping values of 500 for the coarse grid and 150 for the fine grid. These values were calculated by running the inversions with a fixed high *Vp*/*Vs* damping factor. Thereafter, in a similar procedure, the *Vp*/*Vs* damping factor was tested with the fixed chosen *Vp* damping and the final damping values of 700 and 500 produced the best compromise for coarse and fine grids, respectively.

The earthquake hypocenters were kept fixed in the first iteration to avoid any systematic shifts due to setting the station correction to zero. The earthquakes were relocated in the following iterations after the first one (Husen et al., 2003). After the relocation of the hypocenters using the 3-D velocity model, they shifted with a mean of 1 km and a standard deviation of ±1 km in the horizontal direction (mostly in the N-S direction). The values in the vertical direction are 0 and ±3 km, respectively. The inversion was terminated after a total of seven iterations for coarse and five iterations for fine grids. The final RMS misfit was reduced by 30% after the inversion with fine parameterization compared to the 1-D inversion (Jozi Najafabadi et al., 2021). The final RMS misfit was 0.25 s which is still larger than the average picking error of 0.12 s. This discrepancy could indicate unresolved anomalies at a scale smaller than the node spacing which are not recoverable.

4. Resolution Assessment

The assessment of the solution quality is crucial to recognize the volumes of high, poor, or no resolution, smearing effects, and artifacts that might inadvertently cause improper interpretation. Only with the analysis of the solution quality, meaningful interpretations of the results can be made. Moreover, validation of the model parameterization and damping is essential.

The absolute resolution of a volume strongly depends on the density and geometry of the rays passing through that volume. Several parameters such as derivative weighted sum, hit count, resolution diagonal elements, and spread function (Michelini & McEvilly, 1991; Toomey & Foulger, 1989) are measures to assess the resolution. Here, we display the spread function values together with the smearing contours of the model resolution matrix (MRM; Eberhart-Phillips & Michael, 1998). Furthermore, we validate the chosen inversion strategy, parameterization, and damping using the classical checkerboard test as well as a synthetic test with a characteristic 3-D velocity model (expected real structures based on previous studies).

4.1. Spread Function

The spread function synoptically analyzes the information in each row of the MRM. Nodes with low spread values indicate good resolution, whereas the larger the spread value, the less well-resolved the particular node. High values of the spread function indicate smearing; however, it does not provide information on the direction of smearing. To show the directions, we plot the 70% smearing contour (following e.g., Diehl et al., 2009; Haberland et al., 2009; Haberland et al., 2014) for each node which is obtained by normalizing the corresponding row of the MRM by the value of the diagonal element. The well-resolved nodes with no smearing have circled contours around the center, whereas other nodes (mainly nodes with fewer crossing rays) tend to be smeared by neighboring nodes and show elongated contours (Eberhart-Phillips & Michael, 1998; Reyners et al., 1999; Toomey & Foulger, 1989).

Utilizing the spread value, we can distinguish the very well-resolved regions from those that are poorly resolved. However, since its range depends on the data set, parameterization, and regularization, there is no universally applicable threshold for the spread value (Toomey & Foulger, 1989).

Figures 4a and 4b show the spread values and the smearing contours of *Vp* and *Vp*/*Vs*, respectively. The *Vp* spread values from the surface down to 20 km depth are quite low and the well-resolved area is larger at the shallower layers. This resolution geometry is dominated by the seismicity distribution which is mostly restricted to the uppermost 20 km of the crust. Small spread values indicating excellent resolution are found in the volume with high seismicity. Reduced, nevertheless acceptable, resolution at a depth range of 30–45 km in the central volume of the region is indicated by moderate spread values. This is a consequence of diving Pn phases in these parts of the model. Below 50 km depth, no resolution is expected.

Likewise, the *Vp*/*Vs* model is well-resolved at the depth layers of 0, 5, and 10 km. At the 20 km depth layer, the *Vp*/*Vs* model is fairly resolved and below which the resolved area is significantly reduced. The Alpine area is one of the excellent examples, in which the direct Sg (Pg), the Moho-reflected SmS (PmP), and the Moho-refracted

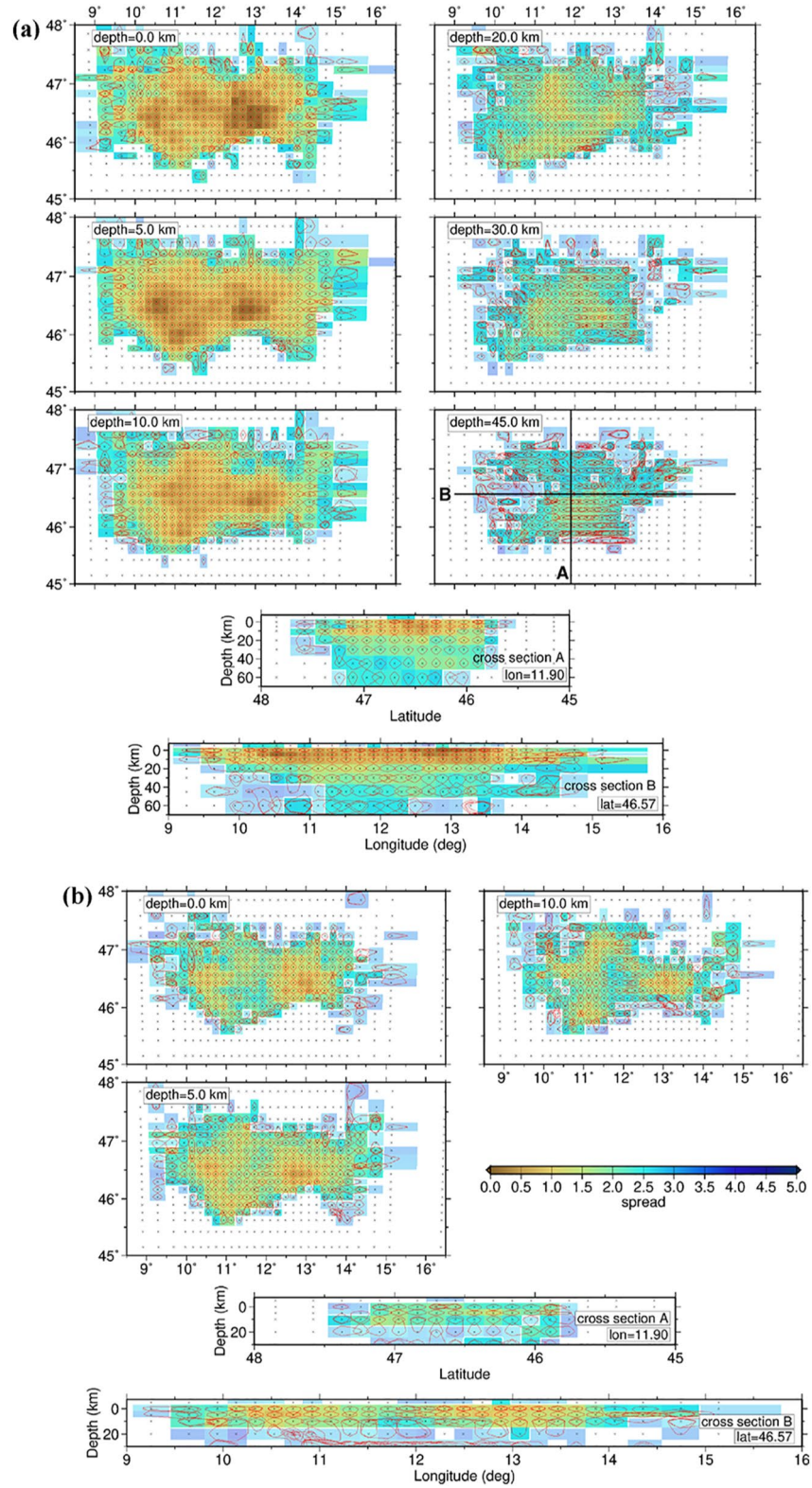

Figure 4. Spread values and the 70% smearing contours (red lines) of the *Vp* (a) and *Vp*/*Vs* (b) models. The unresolved regions (with no ray coverage) are masked with white color and the poorly resolved areas (with spread value smaller than the threshold of 2.7) are faded. The black crosses denote the grid. The location of cross-sections is shown in the depth slice of 45 km in (a). Note that the depth scales in (a) and (b) are different.

Sn (Pn) waves arrive closely spaced in time. However, our data set has only very few Sn arrivals (see e.g., Figure A1) mainly due to the short observational period of only 2 years.

The spread value of 2.7 was empirically defined as a reasonable threshold that fairly separates well-from poorly resolved volumes (also considering the recovery from synthetic tests; see below). The areas with spread values lower than this threshold illustrate minor smearing. However, in general, the E-W smearing is more considerable than N-S and vertical smearing, which we interpret as a consequence of the stations and earthquake geometry. Due to the short maximum distance between the stations and earthquakes in the N-S direction, the number of observed Pn arrivals in this direction is reduced. Therefore, the solution in the deeper parts is influenced mostly by the E-W Pn rays and consequently, the model is smeared in this direction.

4.2. Checkerboard Test

Checkerboard tests intuitively assess the solution quality and are quite common in tomographic inversions to analyze the blurring and smearing in the final model. Given the fine parameterization, we constructed a checkerboard model with the alternating anomalies spanning over two nodes in the *x*-direction and *y*-direction. Between the alternating anomalies, two nodes were left unperturbed to check the horizontal smearing. The alternating anomalies are placed at depths of 0, 10, 30, and 60 km with swapped polarities of the anomalies, and the other layers were left unperturbed to check the vertical smearing. The velocity perturbation includes ±10% of the 1-D model for *Vp* and ±5% for the *Vp*/*Vs* model (Table 2). The synthetic travel times were computed using the forward calculation of the SIMUL2000 code and the same source-receiver distribution as the real data. Random noise was added to the synthetic travel times using the corresponding picking errors for each quality class (see Table 1). Similar to the real data inversion, we used the graded inversion approach and determined the damping values using the trade-off curves.

As can be inferred from Figure 5, the *Vp* anomalies are very well-resolved for the grid nodes with spread values less than 2.7. The high/low input anomalies are well recovered at depth layers of 0 and 10 km with minor vertical smearing at 5 and 20 km depth layers. The horizontal smearing is, however, very small down to a depth of 20 km. Below 20 km the vertical and horizontal smearing is higher, and the well-recovered area is smaller (similar to the resolved region indicated by small spread values; Figure 4). Below ∼50 km depth, no recovery of the anomalies in the checkerboard is expected. This was already inferred from the spread function (Figure 4) that the resolution below 50 km depth is low to non-existent. The geometry and amplitude of the *Vp*/*Vs* anomalies are well recovered down to 10 km depth with minor vertical smearing (Figure 5) and fairly resolved at 20 km depth. Since the number of S arrivals from large epicentral distances in this data set is limited, in particular Sn arrivals, we do not expect a good recovery of the *Vp*/*Vs* below 20 km.

For further assessments, two additional checkerboard tests were conducted. In the first one, altering anomalies of *Vp* and *Vp*/*Vs* were placed at depths of 5, 20, and 45 km, while leaving the 0, 10, and 30 km layers unperturbed. This test had a similar result as the previous one (Figure 5); that is, very good recovery of the main anomalies with minor smearing within the region with a spread value less than 2.7 and poor or no recovery outside (Figure A2).

In the second test, the alternating high and low *Vp* anomalies were extended over one node with one unperturbed node between the alternating anomalies. The horizontal layers were placed at depths similar to the previous test (Figure 5) and the forward and inverse problems were solved in the same manner. Using this test, we can check the recovery of the *Vp* anomalies in the size of one grid node spacing (15 km). Figure 6 shows that fine-scale *Vp* anomalies are geometrically very well recovered down to a depth of 20 km (where we have the most concentration of the crossing rays). However, the amplitudes are reduced by several percent, especially at deeper sections. In general, the bigger the size of the anomaly, the better its amplitude is recovered. Below 30 km, substantial smearing was observed. In a similar test for the *Vp*/*Vs* model, the geometry of the small-scale anomalies was resolved down to the depth of 10 km, however, the amplitudes were significantly reduced (Figure A3).

4.3. Synthetic Test Using a Close-to-Realistic 3-D Velocity Model

A test attempting to reconstruct a synthetic *Vp* model is important because it allows for checking the potential of our data set in resolving the Moho topography. Our synthetic 3-D *Vp* model is aimed to mimic the realistic structure of the region similar to the synthetic *Vp* model of Jozi Najafabadi et al. (2021). It uses the Moho topography

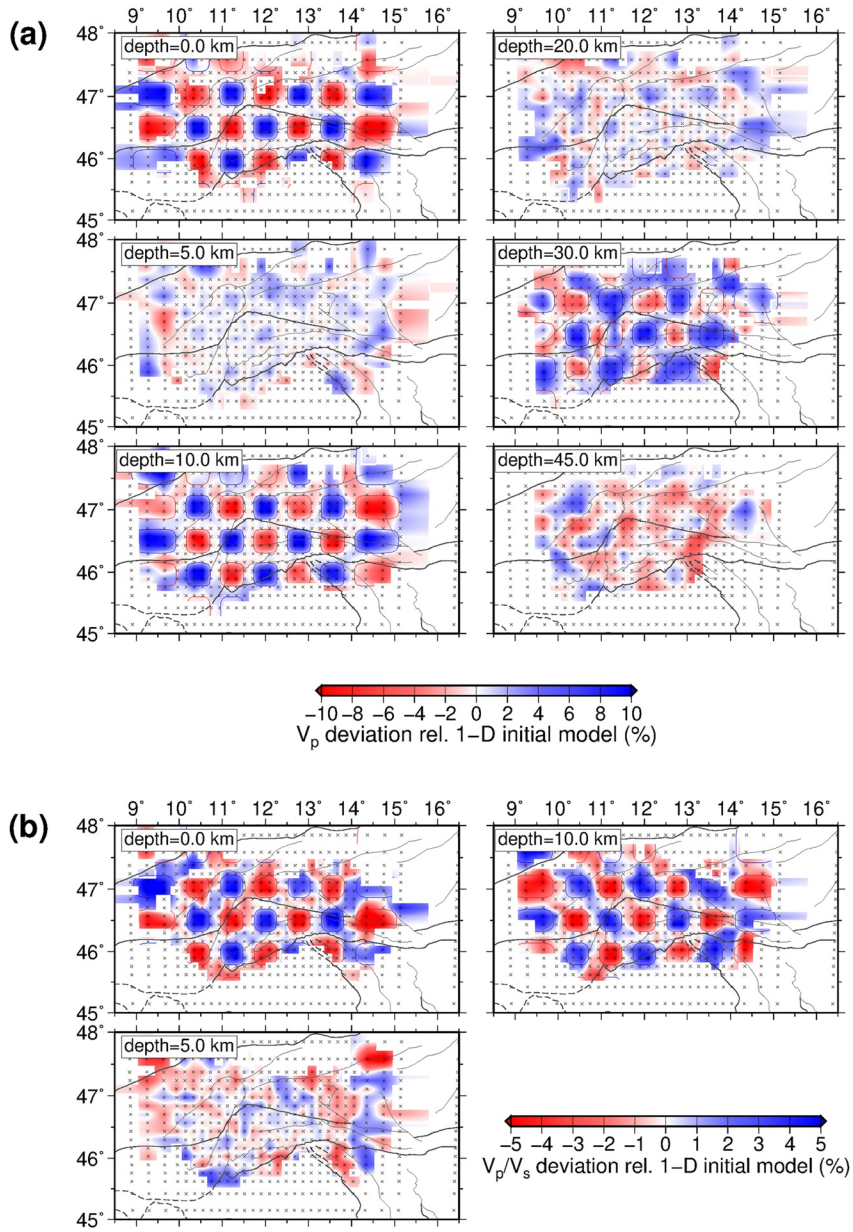

Figure 5. Assessment of the solution quality of the *Vp* (a) and *Vp/Vs* (b) models using classical checkerboard test with alternating anomalies over four nodes of the fine parameterization. The alternating anomalies of *Vp* and *Vp/Vs* were placed at depths of 0, 10, and 30 km, while leaving the 5, 20, and 45 km layers unperturbed. The high and low input anomalies are indicated with blue and red squares, respectively. The crosses mark grid nodes. The unresolved regions (with no ray coverage) are masked with white color. The faded colors denote poorly resolved areas.

of the European and Adriatic Plates following Spada et al. (2013) without features such as the Moho overlap or gap (Figure 7a). The velocity gradually increases from the surface (6 km/s) down to the base of the crust, thereafter, it has a sharp velocity gradient from 7.0 to 8.0 km/s at the Moho depth. For more information on the initial velocity values, the reader is referred to Jozi Najafabadi et al. (2021). Figure 7b illustrates exemplarily the initial synthetic velocity model at the coordinate of 46.5°N/12°E (with a Moho depth of 43 km).

Similar to Waldhauser et al. (2002), the crustal lower velocity anomalies in the PoB, VFB, and MoB sedimentary basins are additionally superimposed on the 3-D model (down to 1-km depth for the PoB and VFB and to 2 km for the MoB; see Jozi Najafabadi et al. [2021] for more information). Unlike the synthetic model of Jozi Najafabadi

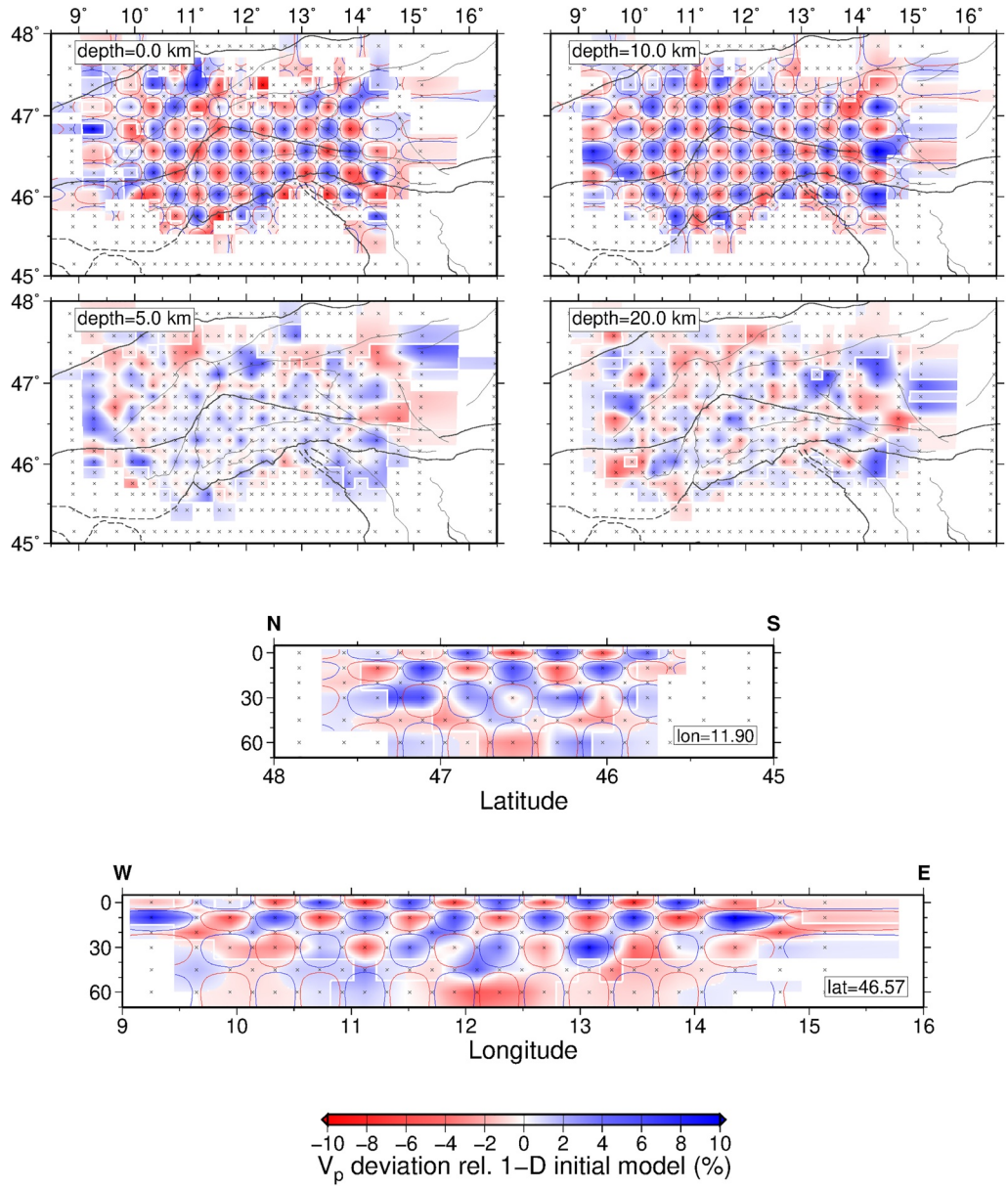

Figure 6. Assessment of the solution quality of the *Vp* model using classical checkerboard test with alternating anomalies over one node of the fine parameterization. Please see Figure 4a (depth slice of 45 km) for locations of the cross-sections and caption of Figure 5 for further features of the figure.

et al. (2021), no high-velocity anomaly for the Tauern Window is considered here, as in the 1-D inversion there were no clear indications for such a signal.

The synthetic P and S arrival times were calculated for the earthquake and station geometry of the real data by using the 3-D FD Eikonal solver (Podvin & Lecomte, 1991; Tryggvason & Bergman, 2006). Synthetic noise was subsequently added to the travel-time data set (individually for each pick quality class; P and S picking uncertainty in Table 1). Ultimately, the synthetic travel times were inverted with the same initial velocities (as shown in Figure 2) and inversion strategy as in the case of real data (Section 3).

Figures 7c–7e show the recovered model after inversion through two N-S and one E-W cross-sections. We have to consider that the velocities in LET are interpolated between the nodes that are predefined by the model parameterization. Therefore, the sharp velocity contrasts (e.g., at the Moho) are broadened and can only be imaged with velocity gradients. It has proven to be useful to define a velocity contour line as a proxy for the velocity contrast

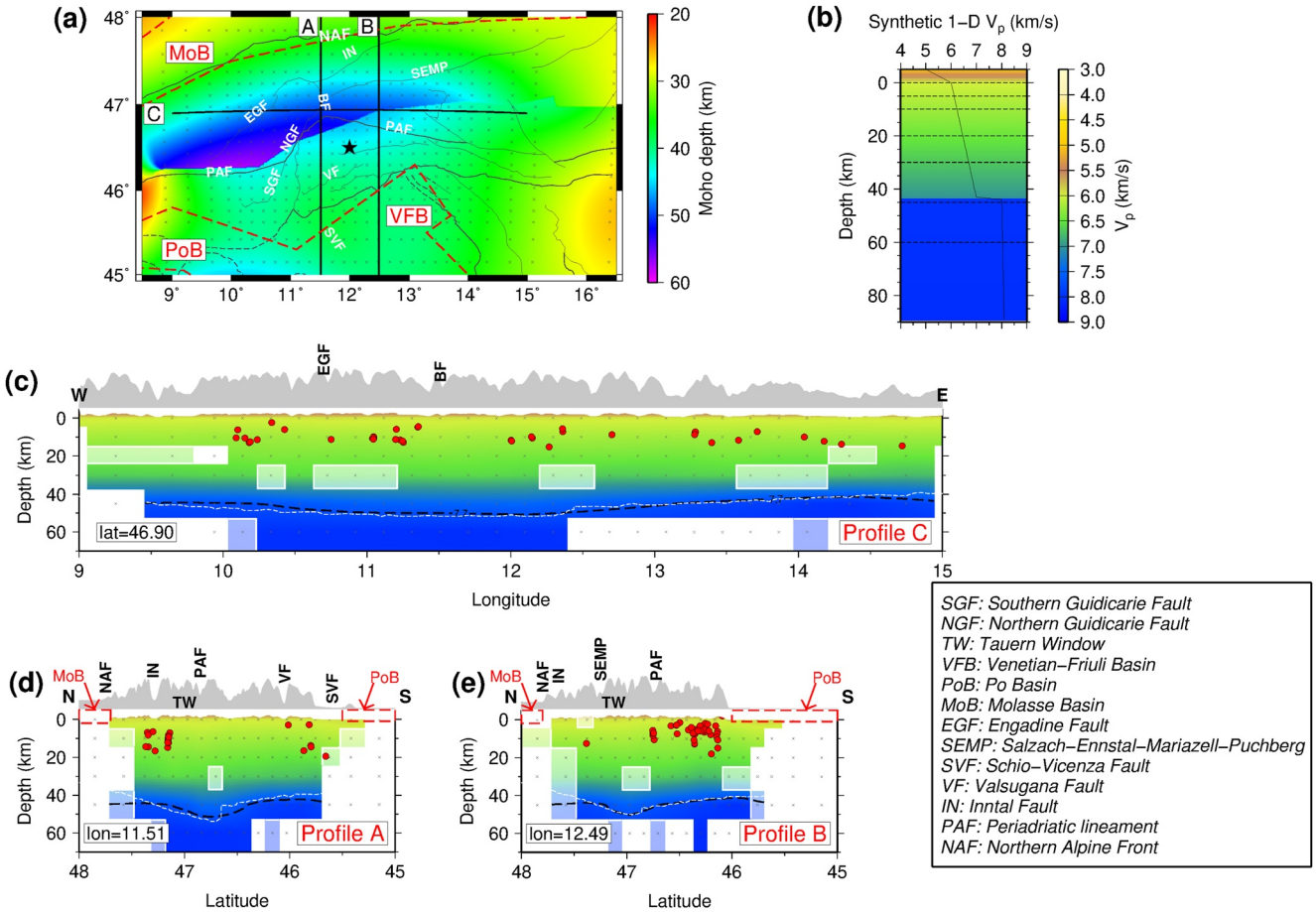

Figure 7. (a) The Moho topography of the region was modified after Spada et al. (2013) (see text for more information). The black star shows an exemplary location for the synthetic 1-D velocity model shown in (b). The dashed red lines illustrate the position of the PoB, VFB, and MoB. (b) An initial 1-D velocity model retrieved from the synthetic 3-D velocity model (the location is shown with a black star in (a)). (c)–(e) The recovered velocity model through one E-W and 2 N-S cross-sections (see (a) for the position of the cross-sections). The dashed black line indicates the Moho proxy with $Vp = 7.7$ km/s. The dashed white line shows the Moho depth after the modified Spada et al. (2013) model (shown in (a)). The earthquakes projected from a swath extending to 15 km on either side of the profiles are shown with red dots. The gray crosses denote the grid nodes. The faded colors denote poorly resolved areas.

expected at the Moho depth (see e.g., Diehl et al., 2009). In our synthetic test, a value of 7.7 km/s (dashed black line) in the inversion result showed the best fit to velocity step in the synthetic (input) model (dashed white line), however, the absolute depths depend on the absolute velocities and the initial model.

The recovered Moho proxy matches the Moho depth of the synthetic model very well in most parts of the resolved areas. The Moho (vertical) offsets are also recovered in terms of depth; however, they are significantly broadened and not sharply defined (due to the grid parameterization, interpolation, and smearing effects).

The low-velocity anomalies in the sedimentary basins of PoB, VFB, and MoB (see dashed red lines in Figure 7) cannot be observed in the recovered model. However, these sedimentary basins are located on the periphery of the network, and the model resolution (ray coverage) does not allow for thoroughly recovering of these anomalies.

No other crustal heterogeneities were included in the synthetic model. The recovered model is smooth without strong artifacts (or smearing) which provides further evidence for the high-resolution capability of our data set.

5. Results

As indicated by the resolution analysis (see above), the strength of our tomographic results lies in imaging the upper and lower crust. The 7.25 km/s iso-velocity line which we treat as a Moho proxy is fairly well recovered beneath the Giudicarie-Lessini region (GL), the TW, and the Inntal region. The *Vp* and *Vp*/*Vs* models as well as

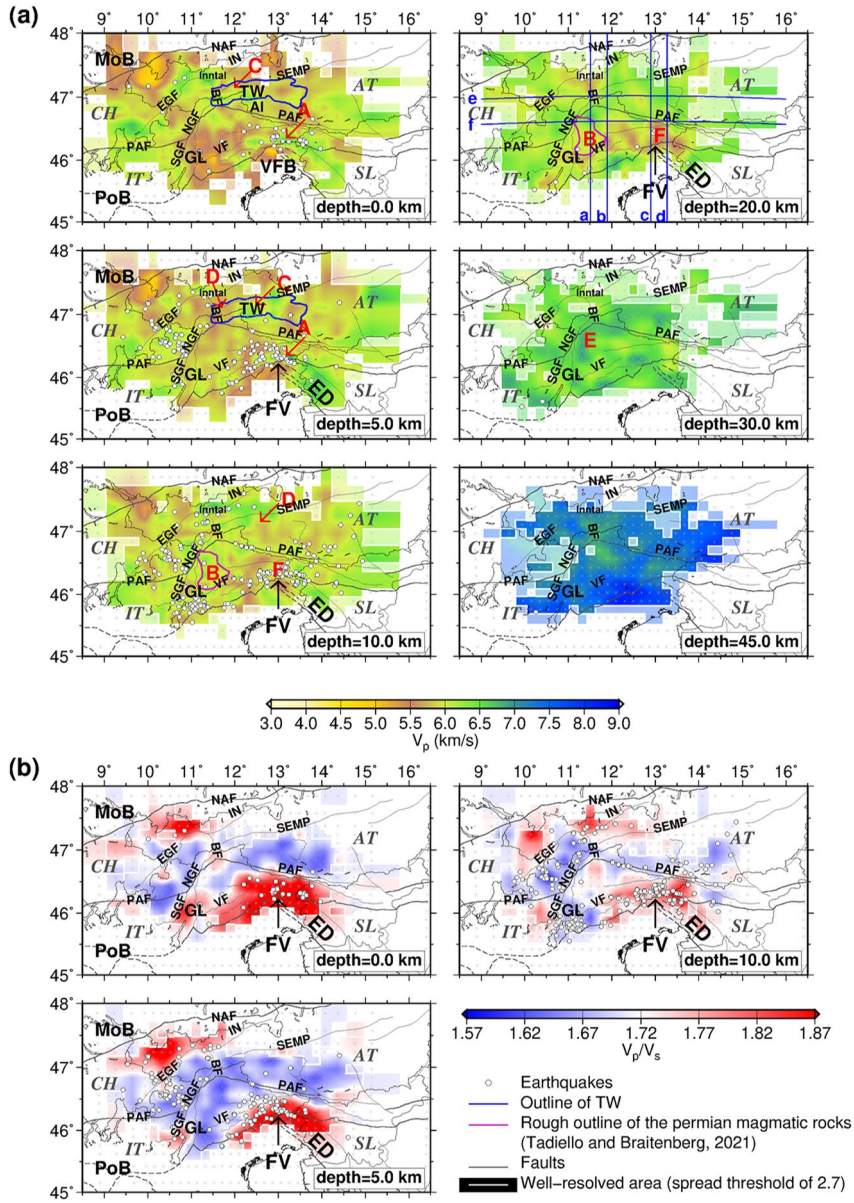

Figure 8. (a) *Vp* velocity model in five horizontal slices. The location of cross-sections in Figure 9 are indicated at the depth slice of 20 km. The *Vp* color scale is consistent with the color scale used in Diehl et al. (2009) and it is set to highlight low velocity regions such as sedimentary basins, intermediate velocities of the crustal domain, and higher velocities in the upper mantle. (b) *Vp/Vp* model in three horizontal slices. The *Vp/Vs* color scale features the model variation relative to initial value considered in the tomography calculation (1.72). Regional faults modified from Schmid et al. (2004), Schmid et al. (2008), and Handy et al. (2010). The faded colors denote poorly resolved areas (spread value smaller than the threshold of 2.7). The anomalies indicated with A, B, C, D, E, and F are discussed in the text. The fault names are given at the depth slice of 0 km in (a). Abbreviations: AI–Adriatic Indenter, BF–Brenner Fault, ED–External Dinarides, EGF–Engadine Fault, FV–Friuli-Venetia region, GL– Giudicarie-Lessini region, IN–Inntal Fault, MoB–Molasse Basin, NAF–Northern Alpine Front, NGF–Northern Giudicarie Fault, PAF–Periadriatic Fault, PoB–Po Basin, SEMP–Salzach-Ennstal-Mariazell-Puchberg, SGF–Southern Giudicarie Fault, TW–Tauern Window, VF–Valsugana Fault, VFB–Venetian-Friuli Basin, IT–Italy, SL–Slovenia, AT–Austria, CH–Switzerland.

the seismicity pattern are shown in the horizontal slices in Figure 8 and vertical cross-sections in Figure 9. These sections illustrate that the velocity in the crust, in particular the upper crust, is both laterally and vertically highly heterogeneous. Several prominent anomalies in the crust can be identified:

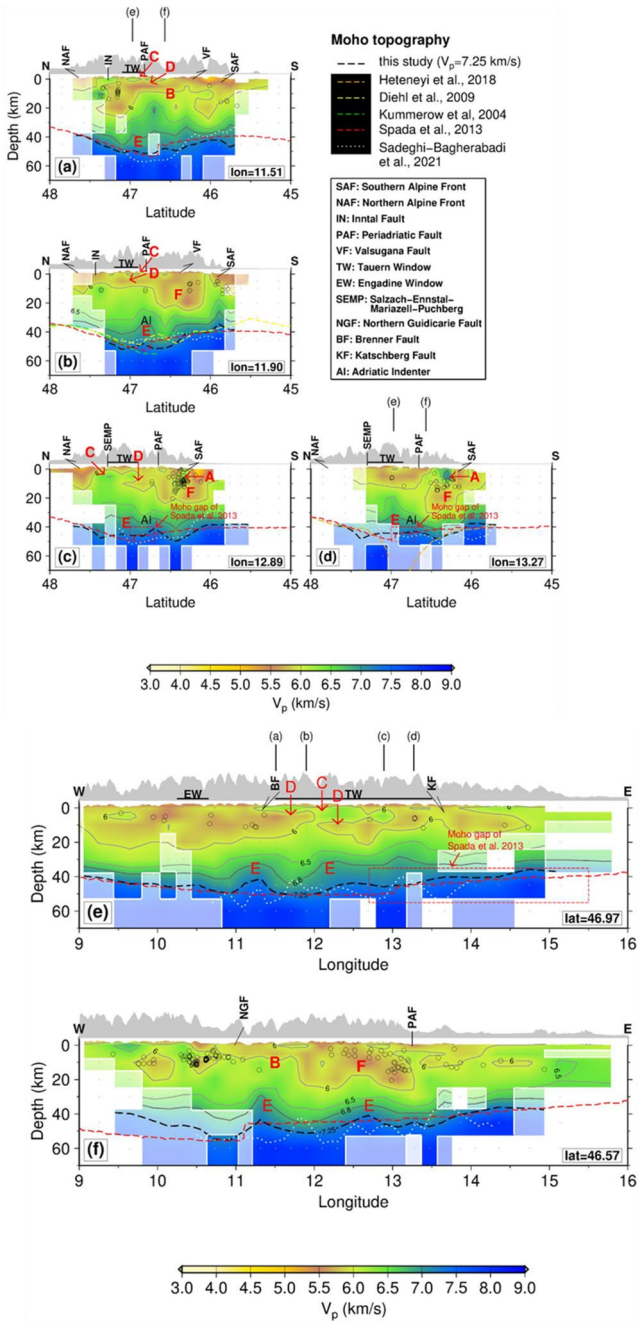

Figure 9. (a)–(d) North-South and (e)–(f) East-West cross-sections of the *Vp* model. See Figure 8a (depth slice of 20 km) for locations of the cross-sections. The hypocenters projected from a swath extending to 15 km on either side of the profiles are shown with black circles. The gray crosses show the grid nodes. The faded colors denote poorly resolved areas (spread value smaller than the threshold of 2.7). The anomalies indicated with A, B, C, D, E, and F are explained in the text. The vertical exaggeration of all the cross-sections is 2:1.

At the surface, reduced *Vp* values (down to 4.6 km/s) are observed in the resolved part of MoB and VFB and high Vp values (~6.5 km/s) are seen in the Friuli-Venetia (FV) region down to a depth of 10 km (anomaly A; Figures 8a, 9c, and 9d). Further toward the east (along the Italian-Slovenian border), there are also elevated P velocities (6.5–6.9 km/s) found. This anomaly seems to be the continuation of anomaly A. However, its SE part extends down to 20 km. This region is also characterized by predominant high values of *Vp*/*Vs* (>1.85). In the upper crust, further increased *Vp* values (6–6.5 km/s) are observed northeast of GL and east of NGF at depth slices of 10 and 20 km (anomaly B; Figures 8a, 9a, and 9f).

The TW region is characterized by a complex velocity structure featuring higher velocities (6–6.5 km/s) at the surface (anomaly C; Figure 8a—depth slices of 0 and 5 km; Figures 9a, 9b, 9c, and 9e) and lower velocities (~5.5 km/s) underneath (anomaly D; Figure 8a—depth slice of 5 km; Figures 9a, 9b, 9c, and 9e).

At 30-km depth (Figure 8a), a prominent high *Vp* anomaly (>6.8 km/s; anomaly E) is observed in the central region of the study area. This anomaly extends from the junction of the SGF and NGF toward the eastern end of the TW (approximately at ~13.5°E; depth slice of 30 km of Figure 8a). This anomaly is best expressed (thickest) south of and beneath the TW and beneath the PAF (see Figure 9).

Figures 9b, 9c, 9d, and 9f reveal a low-velocity region (~5.5 km/s) to the south of the PAF coinciding with the FV region (anomaly F). This implies that in this region, the velocity values corresponding to the upper crust (reddish colors) reach down to a depth of around 25 km, that is, the upper crust is thickened. This anomaly indicates a sharp lateral velocity transition beneath the PAF in the upper crust with higher velocity in the north of the PAF and lower values south of it. However, this transition disappears east of 13.5°E and west of 11.5°E (Figure 9f). Anomaly A with higher velocity (corresponding to the FV region) is located at depths of 0 and 5 km within the anomaly F.

The *Vp*/*Vs* model (Figure 8b) is resolved to a depth of only ~10 km. This is mainly due to the limited number of Sn-picks, so that the deeper parts of the *Vp*/*Vs* model are not well resolved. The *Vp*/*Vs* values vary between 1.57 and 1.87 throughout the study area from the surface down to 10 km depth (Figure 8b). The most prominent feature in the *Vp*/*Vs* model is a zone of high values (>1.85) in the FV. Another zone of increased *Vp*/*Vs* values is observed in the NW of Engadine Fault (SE of MoB); however, this region is at the edge of the resolved volume. As seen in the depth slices of 0 and 5 km of Figure 8a, this region has lower *Vp* values (~4.6 km/s).

LET velocity models are typically relatively smooth and sharp discontinuities (e.g., the Moho) are significantly broadened. Mantle velocities (>8 km/s) are observed at depths >45 km in our tomographic images, with an increased gradient between ~30 and 45 km depth. Therefore, we use an iso-velocity contour of *Vp* = 7.25 km/s to define a proxy for the Moho in these gradual models (dashed black lines in sections of Figure 9; please see also Section 4.3 and Diehl et al., 2009). The Moho proxy is shallower on the Adriatic side (as shallow as 35 km depth) than on the European side (up to ~55 km; see Figures 9a–9c).

The seismicity pattern is very similar to that of Jozi Najafabadi et al. (2021), with earthquakes concentrated mostly in the nappe stack south of the PAF. Seismic activity is observed in the Giudicarie-Lessini region, in the

Engadine area, and in the Austroalpine nappes. The focal depths show that most of the earthquakes occurred down to 22 km depth within the crust. However, the recovered seismicity in our 3-D *Vp* and *Vp*/*Vs* models suggests three earthquakes at the base of the crust in the Giudicarie-Lessini region (depth slices of 30 and 45 km in Figure 8a).

6. Discussion

6.1. Upper Crustal Structure

The low *Vp* anomaly in the MoB (Figure 8a) seems to extend to the south down to a depth of 5 km and is attributed to the marine and freshwater Molasse buried beneath the Helvetic and Penninic units (Ortner et al., 2015; Pomella et al., 2015; Zerlauth et al., 2014). The high *Vp* values of anomaly A in the FV region (Figures 8a, 9c, and 9d) confirm the observation of Diehl et al. (2009) and Brückl et al. (2007) and may be related to dense Mesozoic limestones and dolomitic rocks (Bressan et al., 2012). Velocity values between 6 and 6.8 km/s are expected for the limestones and dolomites (Castagna et al., 1985). Moreover, a prominent cluster of seismicity down to a depth of ∼17 km seems to be associated with this high *Vp* anomaly (Figures 9c and 9d), which is part of the eastern Southern Alpine deformation front. Sadeghi-Bagherabadi et al. (2021) also observed a similar feature in their *Vs* model and showed that a seismic cluster is confined to the S-wave velocity of ∼3.1 and ∼3.6 km/s down to about 20 km.

The *Vp*/*Vs* model in the FV region and external Dinarides (Figure 8b) indicates predominantly high values (>1.85) down to 10 km depth, which fits the values reported for dolomites and limestones (∼1.75 and ∼2.0, respectively; Castagna et al., 1985). However, the amplitude of our *Vp*/*Vs* anomaly becomes smaller at 10 km depth. The *Vp*/*Vs* values in the range of 1.79–1.87 confirm observations of Bressan et al. (2012) and are related to Cretaceous and Jurassic limestones.

The high P-wave velocity body east of NGF (anomaly B) coincides with Permian magmatic rocks in the eastern Southern Alps (purple line at depth slices of 10 and 20 km of Figure 8a; Tadiello & Braitenberg, 2021). This higher velocity anomaly may indicate the continuation of Permain magmatic rocks down to the base of the upper crust. A similar feature was observed in the study by Sadeghi-Bagherabadi et al. (2021) with higher *Vs* values.

The higher P velocities in the region of the TW (anomaly C) can be explained by the European basement nappes (Penninic units) that are exhumed and exposed at the surface (e.g., Rosenberg et al., 2018; Scharf et al., 2013; Schmid et al., 2013). This high-velocity anomaly is underlain by a lower velocity layer in some parts (anomaly D), although the *Vp* rises again at depth of around 15 km. However, resolution of this thin layer is limited by our model parameterization (vertical node spacing of 5 km.

6.2. Lower Crustal Structure

Anomaly E has seismic velocities typical of the lower crust (i.e., 6.8–7.25 km/s; e.g., Holbrook et al., 1992). The boundary between lower and intermediate crust is taken to be the 6.8 km/s iso-velocity line which is obtained by averaging *Vp* measurements of typical intermediate and lower crustal rocks from the Ivrea crustal cross-section exposed in the westernmost Southern Alps (Burke & Fountain, 1990). The lower crust defined this way is anomalously thick in the central part of our study area, a feature which we refer to as the lower crustal "bulge." Figure 10 focuses on this lower crustal bulge and its bearing on previously proposed structural models along the TRANSALP transect.

Two models, the so-called "Crocodile" and "Lateral Extrusion" models, based on active-source reflection seismology (Castellarin et al., 2006; Gebrande et al., 2006; Lüschen et al., 2004, 2006) as well as line drawings from Vibroseis and explosive seismic reflections of Gebrande et al. (2006) are shown in Figures 10a and 10b, respectively. Both models feature a wedge of Adriatic lower crust within the orogenic crust. However, the wedge is more pronounced in the "Lateral Extrusion" model. This model derives its name from the proposed connection at depth of conjugate, oblique-slip faults (the IN, SEMP, and PAF faults; see Figure 8a) that together accommodated eastward motion of the exhumed orogenic crust in the Tauern Window in the latest Oligocene to Miocene time (e.g., Favaro et al., 2017; Scharf et al., 2013).

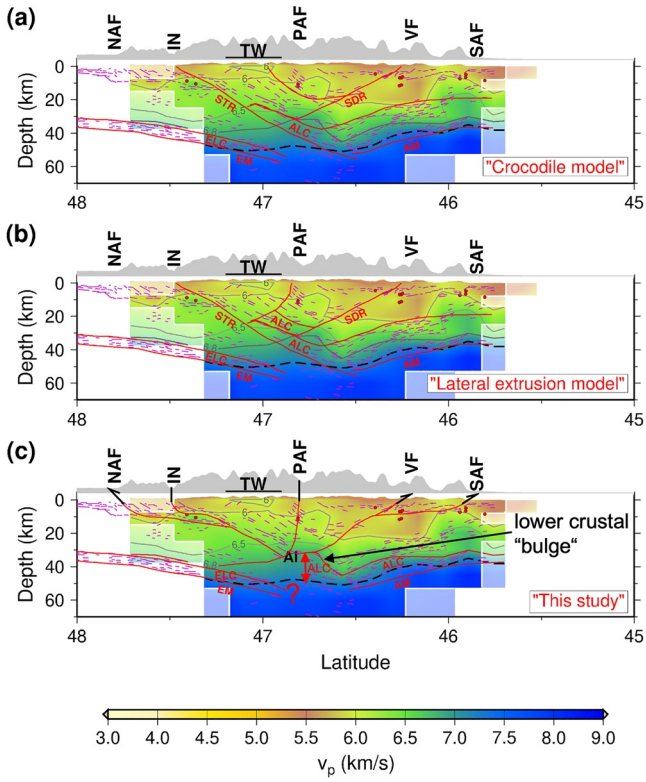

Figure 10. The P-wave velocity model over an N-S vertical cross-section perpendicular to the strike of the Alpine orogen (at 12°E–TRANSALP transect). The faded colors denote poorly resolved areas (spread value smaller than the threshold of 2.7). The dashed black line and the pink lines illustrate the iso-velocity contour of 7.25 km/s (Moho proxy) and the line drawings from Vibroseis and explosive seismic reflections of Gebrande et al. (2006), respectively. The solid red lines in (a) and (b) indicate the evolutionary models of "Crocodile" and "Lateral Extrusion" (Castellarin et al., 2006; Gebrande et al., 2006; Lüschen et al., 2004, 2006), respectively. The solid red lines in (c) illustrate our alternative interpretation based on our LET model and the iso-velocity contour of 6.8 km/s as the upper boundary of the lower crust (see text), and also using the line drawings of Gebrande et al. (2006). The question mark denotes the debatable origin of the Moho (Adriatic or European) beneath PAF. Abbreviations: AI–Adriatic Indenter, ALC–Adriatic Lower Crust, AM–Adriatic Moho, ELC–European Lower Crust, EM–European Moho, IN–Inntal Fault, NAF–Northern Alpine Front, PAF– Periadriatic Fault, SAF–Southern Alpine Front, SDR–Sub-Dolomites Ramp, STR–Sub-Tauern Ramp, TW–Tauern Window, VF–Valsugana Fault.

Our tomographic images in the TRANSALP section indicate that the lower crustal bulge is located mainly beneath and south of the PAF and south of a prominent S-dipping thrust zone, the "Sub-Tauern Ramp (STR)." As interpreted in Figures 10a and 10b, the STR reaches from the Inntal Fault southward some 80 km (Gebrande et al., 2006). This large thrust zone is thought to be associated with the main collisional phase of N-directed thrusting (Schmid et al., 2013; their Figure 6). The age and origin of the lower crustal bulge are unknown; it could be made up of either European or Adriatic lower crust depending on how the faults beneath the Tauern Window are drawn. In Figure 10c, we interpret the tip of the bulge to truncate and therefore postdate the STR. In this scenario, the lower crust detached from its Adriatic upper mantle and protruded to the north. It was emplaced directly onto the downgoing European lower crust. The lower crustal bulge would thus form the northern limit of the Adriatic Indenter at depth. It is tempting to relate this protrusion or wedge to N-S-directed shortening, exhumation, and lateral extrusion of the Penninic units in the TW in Miocene time. Our model contrasts with both models of TRANSALP, which envision emplacement of Adriatic lower crust at shallower depth onto European intermediate crust (e.g., Castellarin et al., 2006; Gebrande et al., 2006). We emphasize that our interpretation does not represent a unique solution. Other interpretations involving both European and Adriatic lower crust are currently being tested by comparing the volume of the lower crustal bulge with estimates of shortening in the Eastern and Southern Alps.

In the Western and Central Alps along the NFP-20E transect, Kissling et al. (2006) imaged a much thinner lower crustal wedge than the bulge depicted in Figure 10c. It has been proposed that this wedge comprises the Adriatic lower crust that was inserted northwards during Oligo-Miocene collision beneath S-directed back-folded and back-thrusted upper crust (Schmid et al., 1996, 1997).

6.3. Crust-Mantle Discontinuity

The crust-mantle velocity discontinuity (Moho) is approximated by an iso-velocity contour at $Vp = 7.25$ km/s, similar to the Moho proxy adopted by Diehl et al. (2009). This yields a Moho depth that is consistent with that obtained from other methods (e.g., controlled-source seismology, receiver functions, local earthquake tomography (LET), and S-wave velocity; Diehl et al., 2009; Hetényi, Plomerová, et al., 2018; Kummerow et al., 2004; Sadeghi-Bagherabadi et al., 2021; Spada et al., 2013). Our Moho proxy (dashed black line in the cross-sections of Figure 9 and iso-velocity contour of Figure 11) changes depth south of the PAF, indicating a significantly shallower Adriatic Moho than European Moho. This is consistent with the southward subduction of the European lithosphere.

Other methods reveal an upward step or a gap in the Moho going from Europe in the north to Adria in the south. For example, Kummerow et al. (2004) imaged a step from ~55 km depth on the European side to ~44 km depth on the Adriatic side at ~46.6°N (Figure 9b). Spada et al. (2013) used a weighted inversion of four methods (Receiver Functions, LET, Controlled-Source Seismology, and Ambient Noise Tomography) to image a similarly sharp Moho offset (Figures 9a–9f). Finally, Sadeghi-Bagherabadi et al. (2021) discerned a Moho that is ~10 km shallower than our Moho proxy between 46.3° and 46.8°N along the TRANSALP transect (Figure 9b). The Moho of Sadeghi-Bagherabadi et al. (2021) is broadly consistent with our Moho proxy along the EASI transect (Figure 9d).

In general, our Moho proxy agrees with several previous studies in the European and Adriatic forelands (Diehl et al., 2009; Hetényi, Plomerová, et al., 2018; Kummerow et al., 2004; Sadeghi-Bagherabadi et al., 2021; Spada

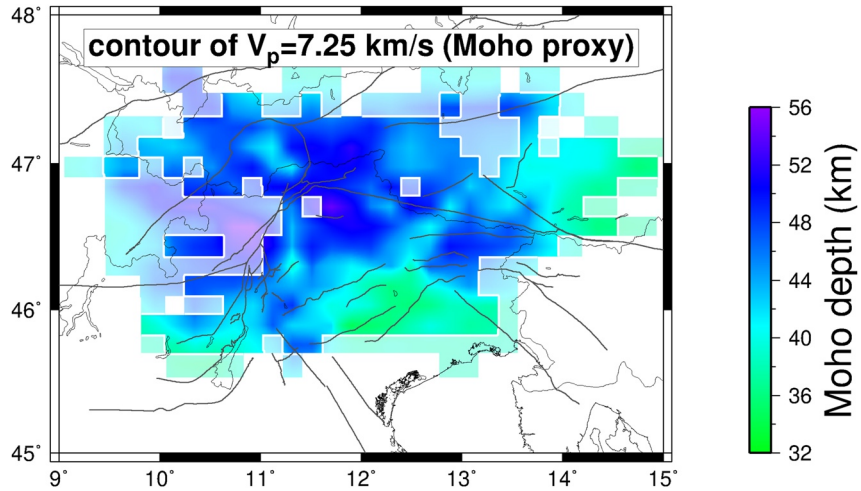

Figure 11. Moho depth based on the iso-velocity contour of *Vp* = 7.25 km/s. The unresolved region is masked with white color and the poorly resolved areas (with spread value smaller than the threshold of 2.7) are faded.

et al., 2013). However, discrepancies are seen beneath the TW and PAF. Due to vertical and horizontal velocity gradients in LET (instead of a velocity contrast, e.g., in receiver functions), it is difficult to clearly differentiate the Adriatic and European Moho or recognize their current position at depth (also indicated with a question mark in Figure 10c). Therefore, other findings, for example, from seismic reflection and receiver functions are needed to provide further insight into the Adria-Europe collision.

7. Conclusion

The high-quality arrival-time data set from dense seismic networks in the Eastern and eastern Southern Alps and the well-constrained hypocenters (Jozi Najafabadi et al., 2021) allowed us to calculate high-resolution 3-D models of *Vp* and *Vp*/*Vs* down to depths of 50 and 10 km, respectively. In the *Vp* model, the upper crust is clearly resolved. Moreover, the lower crust defining the front of the Adriatic Indenter in the Eastern Alps is well observed in the tomographic images. The reliability of the derived crust-mantle discontinuity was studied using a synthetic test with a close-to-realistic 3-D velocity model. The tested Moho topography was recovered without strong artifacts or smearing in the well-resolved region. It is indicated by an increased velocity gradient instead of a discontinuity.

A high-velocity anomaly (6.8–7.25 km/s), found at a depth of about 30–50 km from the NGF toward the eastern end of the TW and imaged in this detail for the first time, indicates thickening of the lower crust beneath and south of the TW and PAF. Our tomographic *Vp* model supports several models of indentation, including one that we propose here in which the lower crustal bulge represents the tip of the Adriatic Indenter and comprises mostly Adriatic lower crust. The lower crust detached from its mantle and upper crust and protruded to the north. We think that thickening and northward indentation of the lower crust may have triggered exhumation and eastward lateral escape of the previously accreted European nappes in the TW. Tectonic balancing of late Oligocene to recent shortening may yield further insight into the make-up of the lower crustal bulge (European, Adriatic, or both?) beneath the Eastern and eastern Southern Alps.

The Moho topography as indicated by an iso-velocity contour of *Vp* = 7.25 km/s (Moho-proxy), derived from our LET, confirms previous findings of a shallower Adriatic Moho (32–40 km) than the European Moho (>45 km). The change in the Moho depth between the two plates generally coincides with a Moho step or gap as imaged with other seismological methods. Our new model is consistent with south-directed subduction of the European lithosphere beneath the Adriatic lithosphere in the Eastern Alps.

Appendix A

Figures A1, A2 and A3

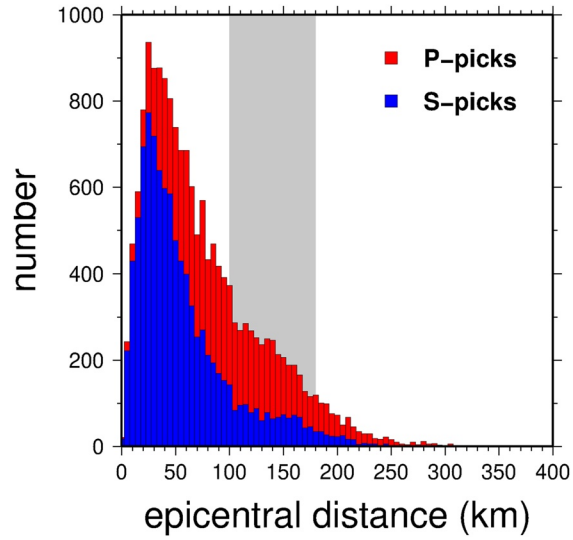

Figure A1. Histogram of the arrival-time data set (P and S picks) as a function of epicentral distance. The gray zone shows the expected cross-over distance (the distance from the earthquake at which the Pn Moho refracted arrival overtakes the Pg directed arrival) for all the earthquakes. The cross-over distance depends on the earthquake depth and Moho depth.

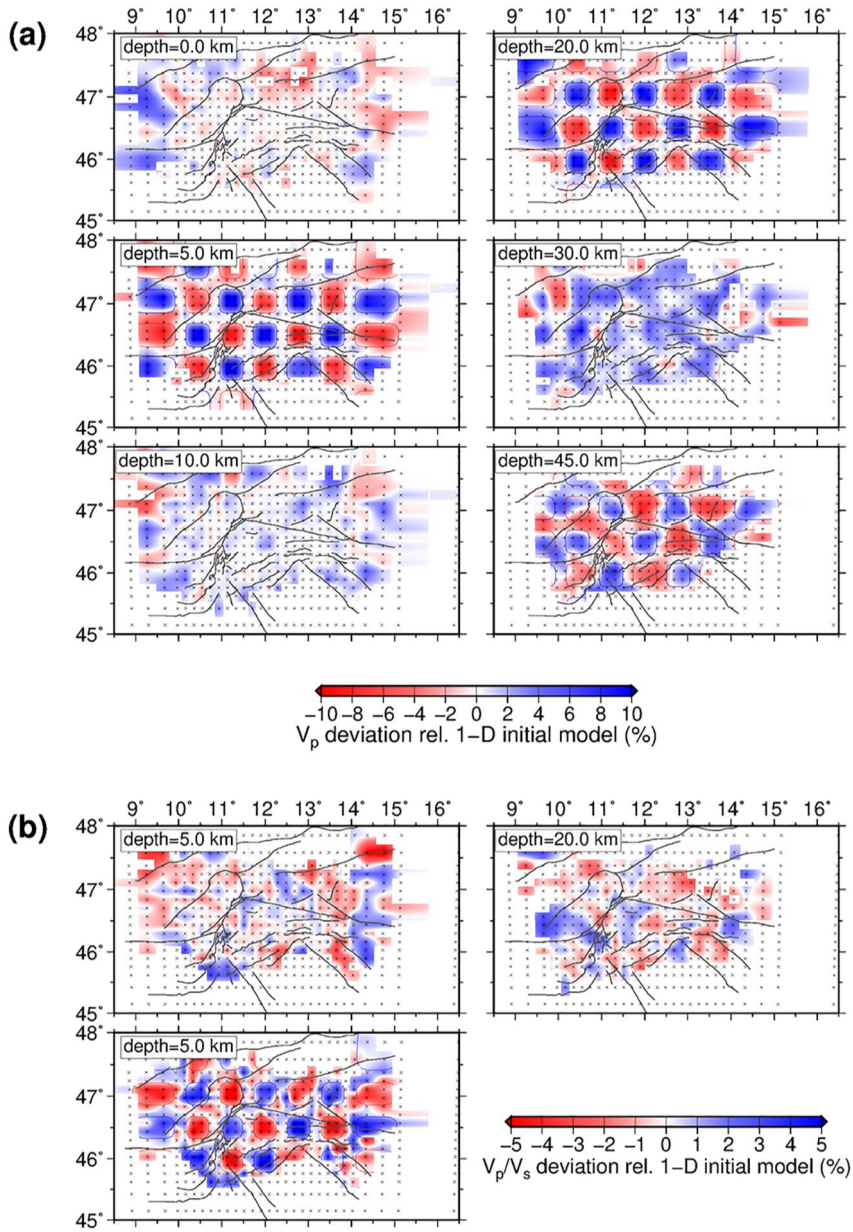

Figure A2. Assessment of the solution quality of the *Vp* (a) and *Vp/Vs* (b) models using classical checkerboard test with alternating anomalies over four nodes of the fine parameterization. This test resembles the test in Figure 5, however, the altering anomalies of *Vp* and *Vp/Vs* were placed at depths of 5, 20, and 45 km, while leaving the 0, 10, and 30 km layers unperturbed. Please see the caption of Figure 5 for further features of the figure.

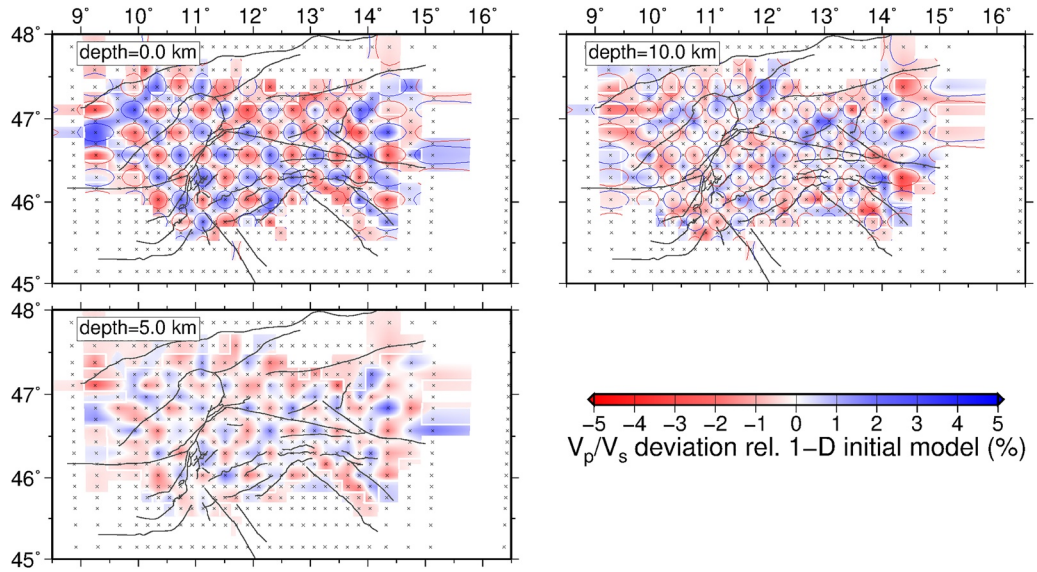

Figure A3. Assessment of the solution quality of the *Vp/Vs* model using classical checkerboard test with alternating anomalies over one node of the fine parameterization. The altering anomalies were placed at depths of 0 and 10 while leaving the 5 km layer unperturbed. Please see the caption of Figure 5 for further features of the figure.

Appendix B: Team List

The AlpArray Seismic Network Team: György Hetényi, Rafael Abreu, Ivo Allegretti, Maria-Theresia Apoloner, Coralie Aubert, Simon Besançon, Maxime Bès De Berc, Götz Bokelmann, Didier Brunel, Marco Capello, Martina Čarman, Adriano Cavaliere, Jérôme Chèze, Claudio Chiarabba, John Clinton, Glenn Cougoulat, Wayne C. Crawford, Luigia Cristiano, Tibor Czifra, Ezio D'alema, Stefania Danesi, Romuald Daniel, Anke Dannowski, Iva Dasović, Anne Deschamps, Jean-Xavier Dessa, Cécile Doubre, Sven Egdorf, Ethz-Sed Electronics Lab, Tomislav Fiket, Kasper Fischer, Wolfgang Friederich, Florian Fuchs, Sigward Funke, Domenico Giardini, Aladino Govoni, Zoltán Gráczer, Gidera Gröschl, Stefan Heimers, Ben Heit, Davorka Herak, Marijan Herak, Johann Huber, Dejan Jarić, Petr Jedlička, Yan Jia, Hélène Jund, Edi Kissling, Stefan Klingen, Bernhard Klotz, Petr Kolínský, Heidrun Kopp, Michael Korn, Josef Kotek, Lothar Kühne, Krešo Kuk, Dietrich Lange, Jürgen Loos, Sara Lovati, Deny Malengros, Lucia Margheriti, Christophe Maron, Xavier Martin, Marco Massa, Francesco Mazzarini, Thomas Meier, Laurent Métral, Irene Molinari, Milena Moretti, Anna Nardi, Jurij Pahor, Anne Paul, Catherine Péquegnat, Daniel Petersen, Damiano Pesaresi, Davide Piccinini, Claudia Piromallo, Thomas Plenefisch, Jaroslava Plomerová, Silvia Pondrelli, Snježan Prevolnik, Roman Racine, Marc Régnier, Miriam Reiss, Joachim Ritter, Georg Rümpker, Simone Salimbeni, Marco Santulin, Werner Scherer, Sven Schippkus, Detlef Schulte-Kortnack, Vesna Šipka, Stefano Solarino, Daniele Spallarossa, Kathrin Spieker, Josip Stipčević, Angelo Strollo, Bálint Süle, Gyöngyvér Szanyi, Eszter Szűcs, Christine Thomas, Martin Thorwart, Frederik Tilmann, Stefan Ueding, Massimiliano Vallocchia, Luděk Vecsey, René Voigt, Joachim Wassermann, Zoltán Wéber, Christian Weidle, Viktor Wesztergom, Gauthier Weyland, Stefan Wiemer, Felix Wolf, David Wolyniec, Thomas Zieke, Mladen Živčić, Helena Žlebčíková. The AlpArray SWATH-D Network Team: Luigia Cristiano, Peter Pilz, Camilla Cattania, Francesco Maccaferri, Angelo Strollo, Susanne Hemmleb, Stefan Mroczek, Thomas Zieke, Günter Asch, Peter Wigger, James Mechie, Karl Otto, Patricia Ritter, Djamil Al-Halbouni, Alexandra Mauerberger, Ariane Siebert, Leonard Grabow, Xiaohui Yuan, Christoph Sens-Schonfelder, Jennifer Dreiling, Rob Green, Lorenzo Mantiloni, Jennifer Jenkins, Alexander Jordan, Azam Jozi Najafabadi, Susanne Kallenbach (Helmholtz-Zentrum Potsdam Deutsches GeoForschungsZentrum [GFZ]), Ludwig Kuhn, Florian Dorgerloh, Stefan Mauerberger, Jan Seidemann (Universität Potsdam), Rens Hofman (Freie Universität Berlin), Helmut Hausmann, Nikolaus Horn, Stefan Weginger, Anton Vogelmann (Austria: Zentralanstalt für Meteorologie und Geodynamik [ZAMG]), Simone Kasemann (Universität Bremen), Claudio Carraro, Corrado Morelli (Südtirol/Bozen: Amt für Geologie und Baustoffprüfung), Günther Walcher, Martin Pernter, Markus Rauch (Civil Protection Bozen), Giorgio Duri, Michele Bertoni, Paolo Fabris (Istituto Nazionale di Oceanografia e di Geofisica

Sperimentale [OGS] [CRS Udine]), Andrea Franceschini, Mauro Zambotto, Luca Froner, Marco Garbin (also OGS; Ufficio Studi Sismici e Geotecnici-Trento).

Data Availability Statement

The SWATH-D waveform data and associated metadata are archived at the GEOFON seismological archive, FDSN code ZS (2017–2019; Heit et al., 2017; doi:10.14470/MF7562601148; last access: December 24, 2021) and are embargoed until August 2023. Data of permanent and temporary AASN networks (network codes: BW, CH, GR, IV, MN, NI, OE, OX, RF, SI, SL, ST, and Z3) are available at the European Integrated Data Archive (EIDA; detailed information in http://www.alparray.ethz.ch/en/seismic_network/backbone/data-access/, last access: August 20, 2021).

Acknowledgments
This research and the SWATH-D seismic network have been supported by the German Science Foundation DFG under Grant nos. HA 3326/5-1, HA 3326/4-1, TI 316/6-1, and WE 1457/22-1 through the special priority programme (SPP) "Mountain Building Processes in Four Dimensions (4D-MB)." The authors thank the Geophysical Instrument Pool Potsdam (GIPP) for facilitating the seismic equipment used for the SWATH-D network in this project (GIPP Grant no. GIPP201717). The authors would like to express our appreciation to all people involved in the instrument preparation, field work, and data archiving (AlpArray team list: http://www.alparray.ethz.ch/en/seismic_network/backbone/data-policy-and-citation/, last access August 20, 2021; SWATH-D team list: http://www.alparray.ethz.ch/en/research/complementary-experiments/swath-d/data-access-citation/, last access August 20, 2021). Discussions with many colleagues within the priority programme are greatly acknowledged. The authors would like to thank Trond Ryberg for his efforts related to the initial localization and 1-D inversion. The authors also appreciate Tobias Diehl for sharing his velocity color palette table. For plotting of figures, the Generic Mapping Tools (GMT; Wessel et al., 2019) were used. The authors would like to thank associate editor Michael Bostock and two anonymous reviewers for their thorough and constructive remarks which led to significant improvement of the manuscript. Open access funding enabled and organized by Projekt DEAL.

References

Abers, G. A., & Roecker, S. W. (1991). Deep structure of an arc-continent collision: Earthquake relocation and inversion for upper mantle P and S wave velocities beneath Papua New Guinea. *Journal of Geophysical Research: Solid Earth*, *96*(B4), 6379–6401. https://doi.org/10.1029/91JB00145

Bijwaard, H., Spakman, W., & Engdahl, E. R. (1998). Closing the gap between regional and global travel time tomography. *Journal of Geophysical Research: Solid Earth*, *103*(B12), 30055–30078. https://doi.org/10.1029/98JB02467

Bressan, G., Gentile, G., Tondi, R., Franco, R. D., & Urban, S. (2012). Sequential integrated inversion of tomographic images and gravity data: An application to the Friuli area (north-eastern Italy). *Bollettino di Geofisica Teorica ed Applicata*, *53*(2), 191–212.

Brückl, E., Bleibinhaus, F., Gosar, A., Grad, M., Guterch, A., Hrubcová, P., et al. (2007). Crustal structure due to collisional and escape tectonics in the Eastern Alps region based on profiles Alp01 and Alp02 from the ALP 2002 seismic experiment. *Journal of Geophysical Research: Solid Earth*, *112*(B6). https://doi.org/10.1029/2006JB004687

Burke, M. M., & Fountain, D. M. (1990). Seismic properties of rocks from an exposure of extended continental crust–new laboratory measurements from the Ivrea Zone. *Tectonophysics*, *182*(1–2), 119–146. https://doi.org/10.1016/0040-1951(90)90346-A

Castagna, J. P., Batzle, M. L., & Eastwood, R. L. (1985). Relationships between compressional-wave and shear-wave velocities in clastic silicate rocks. *Geophysics*, *50*(4), 571–581. https://doi.org/10.1190/1.1441933

Castellarin, A., Vai, G. B., & Cantelli, L. (2006). The Alpine evolution of the Southern Alps around the Giudicarie faults: A Llate Cretaceous to Early Eocene transfer zone. *Tectonophysics*, *414*(1–4), 203–223. https://doi.org/10.1016/j.tecto.2005.10.019

Dando, B. D. E., Stuart, G. W., Houseman, G. A., Hegedüs, E., Brückl, E., et al. (2011). Teleseismic tomography of the mantle in the Carpathian-Pannonian region of central Europe. *Geophysical Journal International*, *186*(1), 11–31. https://doi.org/10.1111/j.1365-246X.2011.04998.x

Diehl, T. (2008). *3-D seismic velocity models of the Alpine crust from local earthquake tomography* (Doctoral dissertation). ETH Zurich.

Diehl, T., Husen, S., Kissling, E., & Deichmann, N. (2009). High-resolution 3-D P-wave model of the Alpine crust. *Geophysical Journal International*, *179*(2), 1133–1147. https://doi.org/10.1111/j.1365-246X.2009.04331.x

Eberhart-Phillips, D. (1986). Three-dimensional velocity structure in northern California Coast Ranges from inversion of local earthquake arrival times. *Bulletin of the Seismological Society of America*, *76*(4), 1025–1052. https://doi.org/10.1785/BSSA0760041025

Eberhart-Phillips, D. (1990). Three-dimensional P and S velocity structure in the Coalinga region, California. *Journal of Geophysical Research: Solid Earth*, *95*(B10), 15343–15363. https://doi.org/10.1029/JB095iB10p15343

Eberhart-Phillips, D., & Michael, A. J. (1993). Three-dimensional velocity structure, seismicity, and fault structure in the Parkfield region, central California. *Journal of Geophysical Research: Solid Earth*, *98*(B9), 15737–15758. https://doi.org/10.1029/93JB01029

Eberhart-Phillips, D., & Michael, A. J. (1998). Seismotectonics of the Loma Prieta, California, region determined from three-dimensional V p, V p/V s, and seismicity. *Journal of Geophysical Research: Solid Earth*, *103*(B9), 21099–21120. https://doi.org/10.1029/98JB01984

Evans, J., Eberhart-Phillips, D., & Thurber, C. H. (1994). *User's manual for SIMULPS12 for imaging vp and vp/vs; a derivative of the "Thurber" tomographic inversion SIMUL3 for local earthquakes and explosions*. Open-File Report 94-431. U.S. Geological Survey. https://doi.org/10.3133/ofr94431

Favaro, S., Handy, M. R., Scharf, A., & Schuster, R. (2017). Changing patterns of exhumation and denudation in front of an advancing crustal indenter, Tauern Window (Eastern Alps). *Tectonics*, *36*(6), 1053–1071. https://doi.org/10.1002/2016TC004448

Gebrande, H., Lüschen, E., Bopp, M., Bleibinhaus, F., Lammerer, B., Onckenet, O., et al. (2006). Publisher's correction to "First deep seismic reflection images of the Eastern Alps reveal giant crustal wedges and transcrustal ramps". *Geophysical Research Letters*, *33*, L15312. https://doi.org/10.1029/2006GL026618

Haberland, C., Bohm, M., & Asch, G. (2014). Accretionary nature of the crust of Central and East Java (Indonesia) revealed by local earthquake travel-time tomography. *Journal of Asian Earth Sciences*, *96*, 287–295. https://doi.org/10.1016/j.jseaes.2014.09.019

Haberland, C., Rietbrock, A., Lange, D., Bataille, K., & Dahm, T. (2009). Structure of the seismogenic zone of the southcentral Chilean margin revealed by local earthquake traveltime tomography. *Journal of Geophysical Research: Solid Earth*, *114*(B1). https://doi.org/10.1029/2008JB005802

Handy, M. R., Schmid, S. M., Bousquet, R., Kissling, E., & Bernoulli, D. (2010). Reconciling plate-tectonic reconstructions of Alpine Tethys with the geological–geophysical record of spreading and subduction in the Alps. *Earth-Science Reviews*, *102*(3), 121–158. https://doi.org/10.1016/j.earscirev.2010.06.002

Handy, M. R., Schmid, S. M., Paffrath, M., Friederich, W., & the AlpArray Working Group (2021). European lithosphere and slabs beneath the greater Alpine area – Interpretations based on teleseismic P-wave tomography. *Solid Earth*, *12*, 2633–2669. Retrieved from https://se.copernicus.org/articles/12/2633/2021

Handy, M. R., Ustaszewski, K., & Kissling, E. (2015). Reconstructing the Alps–Carpathians–Dinarides as a key to understanding switches in subduction polarity, slab gaps and surface motion. *International Journal of Earth Sciences*, *104*(1), 1–26. https://doi.org/10.1007/s00531-014-1060-3

Heit, B., Cristiano, L., Haberland, C., Tilmann, F., Pesaresi, D., Jia, Y., et al. (2021). The SWATH-D seismological network in the Eastern Alps. *Seismological Society of America*, *92*(3), 1592–1609. https://doi.org/10.1785/0220200377

Heit, B., Weber, M., Tilmann, F., Haberland, C., Jia, Y., & Pesaresi, D. (2017). *The Swath-D seismic network in Italy and Austria*. GFZ Data Services. https://doi.org/10.14470/MF7562601148

Hetényi, G., Molinari, I., Clinton, J., Bokelmann, G., Bondár, I., Crawford, W., et al. (2018). The AlpArray Seismic Network: A large-scale European experiment to image the Alpine Orogen. *Surveys in Geophysics*, *39*(5), 1009–1033. https://doi.org/10.1007/s10712-018-9472-4

Hetényi, G., Plomerová, J., Bianchi, I., Exnerová, H. K., Bokelmann, G., Handy, M. R., & Babuška, V., & AlpArray-EASI Working Group. (2018). From mountain summits to roots: Crustal structure of the Eastern Alps and Bohemian Massif along longitude 13.3 E. *Tectonophysics*, *744*, 239–255. https://doi.org/10.1016/j.tecto.2018.07.001

Holbrook, S., Mooney, W., & Christensen, N. I. (1992). The seismic velocity structure of the deep continental crust. *Continental Lower Crust*, *23*, 1–43.

Horváth, F., Bada, G., Szafián, P., Tari, G., Ádám, A., & Cloetingh, S. (2006). Formation and deformation of the Pannonian Basin: Constraints from observational data. *Geological Society, London, Memoirs*, *32*, 191–206. https://doi.org/10.1144/GSL.MEM.2006.032.01.11

Husen, S., Kissling, E., & Flueh, E. R. (2000). Local earthquake tomography of shallow subduction in north Chile: A combined onshore and offshore study. *Journal of Geophysical Research: Solid Earth*, *105*(B12), 28183–28198. https://doi.org/10.1029/2000JB900229

Husen, S., Quintero, R., Kissling, E., & Hacker, B. (2003). Subduction-zone structure and magmatic processes beneath Costa Rica constrained by local earthquake tomography and petrological modelling. *Geophysical Journal International*, *155*(1), 11–32. https://doi.org/10.1046/j.1365-246X.2003.01984.x

Jozi Najafabadi, A., Haberland, C., Ryberg, T., Verwater, V. F., Le Breton, E., Handy, M. R., & Weber, M., & the AlpArray & AlpArray SWATH-D Working Groups. (2021). Relocation of earthquakes in the southern and eastern Alps (Austria, Italy) recorded by the dense, temporary SWATH-D network using a Markov chain Monte Carlo inversion. *Solid Earth*, *12*(5), 1087–1109. https://doi.org/10.5194/se-12-1087-2021

Karousová, H., Plomerová, J., & Babuška, V. (2013). Upper-mantle structure beneath the southern Bohemian Massif and its surroundings imaged by high-resolution tomography. *Geophysical Journal International*, *194*(2), 1203–1215. https://doi.org/10.1093/gji/ggt159

Kissling, E. (1988). Geotomography with local earthquake data. *Reviews of Geophysics*, *26*(4), 659–698. https://doi.org/10.1029/RG026i004p00659

Kissling, E., Schmid, S. M., Lippitsch, R., Ansorge, J., & Fügenschuh, B. (2006). Lithosphere structure and tectonic evolution of the Alpine arc: New evidence from high-resolution teleseismic tomography. *Geological Society, London, Memoirs*, *32*(1), 129–145. https://doi.org/10.1144/gsl.mem.2006.032.01.08

Koulakov, I., Kaban, M. K., Tesauro, M., & Cloetingh, S. (2009). P- and S-velocity anomalies in the upper mantle beneath Europe from tomographic inversion of ISC data. *Geophysical Journal International*, *179*(1), 345–366. https://doi.org/10.1111/j.1365-246X.2009.04279.x

Kummerow, J., Kind, R., Oncken, O., Giese, P., Ryberg, T., Wylegalla, K., et al. (2004). A natural and controlled source seismic profile through the Eastern Alps: TRANSALP. *Earth and Planetary Science Letters*, *225*(1), 115–129. https://doi.org/10.1016/j.epsl.2004.05.040

Le Breton, E., Brune, S., Ustaszewski, K., Zahirovic, S., Seton, M., & Müller, R. D. (2021). Kinematics and extent of the Piemont–Liguria Basin – Implications for subduction processes in the Alps. *Solid Earth*, *12*(4), 885–913. https://doi.org/10.5194/se-12-885-2021

Le Breton, E., Handy, M. R., Molli, G., & Ustaszewski, K. (2017). Post-20 Ma motion of the Adriatic Plate: New constraints from surrounding Orogens and implications for crust-mantle decoupling. *Tectonics*, *36*(12), 3135–3154. https://doi.org/10.1002/2016TC004443

Lippitsch, R., Kissling, E., & Ansorge, J. (2003). Upper mantle structure beneath the Alpine orogen from high-resolution teleseismic tomography. *Journal of Geophysical Research: Solid Earth*, *108*(B8). https://doi.org/10.1029/2002JB002016

Lüschen, E., Borrini, D., Gebrande, H., Lammerer, B., Millahn, K., Neubauer, F., et al. (2006). TRANSALP—Deep crustal Vibroseis and explosive seismic profiling in the Eastern Alps. *Tectonophysics*, *414*(1), 9–38. https://doi.org/10.1016/j.tecto.2005.10.014

Lüschen, E., Lammerer, B., Gebrande, H., Millahn, K., & Nicolich, R., & TRANSALP Working Group. (2004). Orogenic structure of the Eastern Alps, Europe, from TRANSALP deep seismic reflection profiling. *Tectonophysics*, *388*(1–4), 85–102. https://doi.org/10.1016/j.tecto.2004.07.024

Michelini, A., & McEvilly, T. (1991). Seismological studies at Parkfield. I. Simultaneous inversion for velocity structure and hypocenters using cubic B-splines parameterization. *Bulletin of the Seismological Society of America*, *81*(2), 524–552.

Mitterbauer, U., Behm, M., Brückl, E., Lippitsch, R., Guterch, A., Keller, G. R., et al. (2011). Shape and origin of the East-Alpine slab constrained by the ALPASS teleseismic model. *Tectonophysics*, *510*(1), 195–206. https://doi.org/10.1016/j.tecto.2011.07.001

Nocquet, J. M., & Calis, E. (2004). Geodetic measurements of crustal deformation in the Western Mediterranean and Europe. *Pure and Applied Geophysics*, *161*(3), 661–681. https://doi.org/10.1007/s00024-003-2468-z

Ortner, H., Aichholzer, S., Zerlauth, M., Pilser, R., & Fügenschuh, B. (2015). Geometry, amount, and sequence of thrusting in the Subalpine Molasse of western Austria and southern Germany, European Alps. *Tectonics*, *34*(1), 1–30. https://doi.org/10.1002/2014TC003550

Paffrath, M., Friederich, W., Schmid, S. M., & Handy, M. R., & the AlpArray and AlpArray-Swath Working Group. (2021). Imaging structure and geometry of slabs in the greater Alpine area – A P-wave travel-time tomography using AlpArray Seismic Network data. *Solid Earth*, *12*, 2671–2702. https://doi.org/10.5194/se-12-2671-2021

Pfiffner, O. A., Lehner, P., Heitzmann, P., Mueller, S., & Steck, A. (Eds.) (1997). *Deep structure of the Swiss Alps: Results of NRP 20*. (p. 460). Birkhauser Verlag. https://doi.org/10.1111/j.1365-246X.1997.tb01232.x

Piromallo, C., & Morelli, A. (2003). P wave tomography of the mantle under the Alpine-Mediterranean area. *Journal of Geophysical Research: Solid Earth*, *108*(B2). https://doi.org/10.1029/2002JB001757

Podvin, P., & Lecomte, I. (1991). Finite difference computation of traveltimes in very contrasted velocity models: A massively parallel approach and its associated tools. *Geophysical Journal International*, *105*(1), 271–284. https://doi.org/10.1111/j.1365-246X.1991.tb03461.x

Pomella, H., Klötzli, U., Scholger, R., Stipp, M., & Fügenschuh, B. (2011). The Northern Giudicarie and the Meran-Mauls fault (Alps, Northern Italy) in the light of new paleomagnetic and geochronological data from boudinaged Eo-/Oligocene tonalites. *International Journal of Earth Sciences*, *100*(8), 1827–1850. https://doi.org/10.1007/s00531-010-0612-4

Pomella, H., Ortner, H., Zerlauth, M., & Fügenschuh, B. (2015). The Alpine nappe stack in western Austria: A crustal-scale cross section. *International Journal of Earth Sciences*, *104*(3), 733–745. https://doi.org/10.1007/s00531-014-1097-3

Pomella, H., Stipp, M., & Fügenschuh, B. (2012). Thermochronological record of thrusting and stri-ke-slip faulting along the Giudicarie fault system (Alps, Northern Italy). *Tectonophysics*, *579*, 118–130. https://doi.org/10.1016/j.tecto.2012.04.015

Ratschbacher, L., Frisch, W., Linzer, H. G., & Merle, O. (1991). Lateral extrusion in the eastern Alps, Part 2: Structural analysis. *Tectonics*, *10*(2), 257–271. https://doi.org/10.1029/90TC02623

Reyners, M., Eberhart-Phillips, D., & Stuart, G. (1999). A three-dimensional image of shallow subduction: Crustal structure of the Raukumara Peninsula, New Zealand. *Geophysical Journal International*, *137*(3), 873–890. https://doi.org/10.1046/j.1365-246x.1999.00842.x

Rosenberg, C. L., & Kissling, E. (2013). Three-dimensional insight into Central-Alpine collision: Lower-plate or upper-plate indentation? *Geology*, *41*(12), 1219–1222. https://doi.org/10.1130/G34584.1

Rosenberg, C. L., Schneider, S., Scharf, A., Bertrand, A., Hammerschmidt, K., Rabaute, A., et al. (2018). Relating collisional kinematics to exhumation processes in the Eastern Alps. *Earth-Science Reviews*, *176*, 311–344. https://doi.org/10.1016/j.earscirev.2017.10.013

Ryberg, T., & Haberland, C. (2019). Bayesian simultaneous inversion for local earthquake hypocentres and 1-D velocity structure using minimum prior knowledge. *Geophysical Journal International*, *218*(2), 840–854. https://doi.org/10.1093/gji/ggz177

Sadeghi-Bagherabadi, A., Vuan, A., Aoudia, A., Parolai, S., & the AlpArray and AlpArray-Swath Working Group. (2021). High-resolution crustal S-wave velocity model and Moho geometry beneath the Southeastern Alps: New insights from the SWATH-D experiment. *Frontiers of Earth Science*, *9*(188). https://doi.org/10.3389/feart.2021.641113

Scharf, A., Handy, M. R., Favaro, S., Schmid, S. M., & Bertrand, A. (2013). Modes of orogen-parallel stretching and extensional exhumation in response to microplate indentation and roll-back subduction (Tauern Window, Eastern Alps). *International Journal of Earth Sciences*, *102*(6), 1627–1654. https://doi.org/10.1007/s00531-013-0894-4

Schmid, S. M., Aebli, H. R., Heller, F., & Zingg, A. (1989). The role of the Periadriatic Line in the tectonic evolution of the Alps. *Geological Society, London, Special Publications*, *45*(1), 153–171. https://doi.org/10.1144/gsl.sp.1989.045.01.08

Schmid, S. M., Bernoulli, D., Fügenschuh, B., Matenco, L., Schefer, S., Schuster, R., et al. (2008). The Alpine-Carpathian-Dinaridic orogenic system: Correlation and evolution of tectonic units. *Swiss Journal of Geosciences*, *101*(1), 139–183. https://doi.org/10.1007/s00015-008-1247-3

Schmid, S. M., Fügenschuh, B., Kissling, E., & Schuster, R. (2004). Tectonic map and overall architecture of the Alpine orogen. *Eclogae Geologicae Helvetiae*, *97*(1), 93–117. https://doi.org/10.1007/s00015-004-1113-x

Schmid, S. M., & Kissling, E. (2000). The arc of the western Alps in the light of geophysical data on deep crustal structure. *Tectonics*, *19*(1), 62–85. https://doi.org/10.1029/1999TC900057

Schmid, S. M., Pfiffner, O. A., Froitzheim, N., Schönborn, G., & Kissling, E. (1996). Geophysical-geological transect and tectonic evolution of the Swiss-Italian Alps. *Tectonics*, *15*(5), 1036–1064. https://doi.org/10.1029/96TC00433

Schmid, S. M., Pfiffner, O. A., & Schreurs, G. (1997). Rifting and collision in the Penninic zone of eastern Switzerland. *Deep structure of the Swiss Alps: results of NRP*, 20, 160–185.

Schmid, S. M., Scharf, A., Handy, M. R., & Rosenberg, C. L. (2013). The Tauern Window (Eastern Alps, Austria): A new tectonic map, with cross-sections and a tectonometamorphic synthesis. *Swiss Journal of Geosciences*, *106*(1), 1–32. https://doi.org/10.1007/s00015-013-0123-y

Schuster, R., & Stüwe, K. (2008). Permian metamorphic event in the Alps. *Geology*, *36*(8), 603–606. https://doi.org/10.1130/g24703a.1

Solarino, S., Kissling, E., Sellami, S., Smriglio, G., Thouvenot, F., Granet, M., et al. (1997). Compilation of a recent seismicity data base of the greater Alpine region from several seismological networks and preliminary 3D tomographic results. *Annals of Geophysics*, *XL*(1), Retrieved from http://hdl.handle.net/2122/1542

Spada, M., Bianchi, I., Kissling, E., Agostinetti, N. P., & Wiemer, S. (2013). Combining controlled-source seismology and receiver function information to derive 3-D Moho topography for Italy. *Geophysical Journal International*, *194*(2), 1050–1068. https://doi.org/10.1093/gji/ggt148

Tadiello, D., & Braitenberg, C. (2021). Gravity modeling of the Alpine lithosphere affected by magmatism based on seismic tomography. *Solid Earth*, *12*(2), 539–561. https://doi.org/10.5194/se-12-539-2021

Thurber, C. H. (1983). Earthquake locations and three-dimensional crustal structure in the Coyote Lake area, central California. *Journal of Geophysical Research: Solid Earth*, *88*(B10), 8226–8236. https://doi.org/10.1029/JB088iB10p08226

Thurber, C., & Eberhart-Phillips, D. (1999). Local earthquake tomography with flexible gridding. *Computers & Geosciences*, *25*(7), 809–818. https://doi.org/10.1016/S0098-3004(99)00007-2

Toomey, D., & Foulger, G. (1989). Tomographic inversion of local earthquake data from the Hengill-Grensdalur central volcano complex, Iceland. *Journal of Geophysical Research: Solid Earth*, *94*(B12), 17497–17510. https://doi.org/10.1029/JB094iB12p17497

Tryggvason, A., & Bergman, B. (2006). A traveltime reciprocity discrepancy in the Podvin & Lecomte time3d finite difference algorithm. *Geophysical Journal International*, *165*(2), 432–435. https://doi.org/10.1111/j.1365-246X.2006.02925.x

Um, J., & Thurber, C. (1987). A fast algorithm for two-point seismic ray tracing. *Bulletin of the Seismological Society of America*, *77*(3), 972–986. https://doi.org/10.1785/BSSA0770030972

Verwater, V. F., Le Breton, E., Handy, M. R., Picotti, V., Jozi Najafabadi, A., & Haberland, C. (2021). Neogene kinematics of the Giudicarie Belt and eastern Southern Alpine orogenic front (northern Italy). *Solid Earth*, *12*, 1309–1334. https://doi.org/10.5194/se-12-1309-2021

Viganò, A., Scafidi, D., Martin, S., & Spallarossa, D. (2013). Structure and properties of the Adriatic crust in the central-eastern Southern Alps (Italy) from local earthquake tomography. *Terra Nova*, *25*(6), 504–512. https://doi.org/10.1111/ter.12067

Vrabec, M., & Fodor, L. (2006). Late Cenozoic tectonics of Slovenia: Structural styles at the northeastern corner of the Adriatic microplate. In N. Pinter, G. Grenerczy, J. Weber, S. Stein, & D. Medak (Eds.), *The Adria microplate: GPS geodesy, tectonics and hazards* (Vol. 61, pp. 151–168). Springer. https://doi.org/10.1007/1-4020-4235-3_10

Waldhauser, F., Lippitsch, R., Kissling, E., & Ansorge, J. (2002). High-resolution teleseismic tomography of upper-mantle structure using an a priori three-dimensional crustal model. *Geophysical Journal International*, *150*(2), 403–414. https://doi.org/10.1046/j.1365-246X.2002.01690.x

Wessel, P., Luis, J. F., Uieda, L., Scharroo, R., Wobbe, F., Smith, W. H. F., et al. (2019). The Generic Mapping Tools version 6. *Geochemistry, Geophysics, Geosystems*, *20*(11), 5556–5564. https://doi.org/10.1029/2019GC008515

Zerlauth, M., Ortner, H., Pomella, H., Pfiffner, O. A., & Fügenschuh, B. (2014). Inherited tectonic structures controlling the deformation style: An example from the Helvetic nappes of the eastern Alps. *Swiss Journal of Geosciences*, *107*(2), 157–175. https://doi.org/10.1007/s00015-014-0167-7

Zhao, L., Paul, A., Malusà, M. G., Xu, X., Zheng, T., Solarino, S., et al. (2016). Continuity of the Alpine slab unraveled by high-resolution P wave tomography. *Journal of Geophysical Research: Solid Earth*, *121*(12), 8720–8737. https://doi.org/10.1002/2016JB013310